Geochimica et Cosmochimica Acta 408 (2025) 84–104

Contents lists available at ScienceDirect

Geochimica et Cosmochimica Acta

journal homepage: www.elsevier.com/locate/gca

Hydrogen, single-carbon compounds, and thermal regime in the oceanic ultramafic-dominated lithosphere: insights from a deep borehole on the Atlantis Massif

Susan Q. Lang [a,*], C. Geoffrey Wheat [b], Kristin L. Dickerson [c], Mark K. Reagan [d], Ivan P. Savov [e], Jordyn A. Robare [f], William J. Brazelton [g], Johanna Suhonen [h], Oscar Cavazos [h], Andrew McCaig [e], Peter Blum [h], Natsue Abe [i], Rémi Coltat [j,k], Jeremy R. Deans [l], Marguerite Godard [m], Barbara E. John [n], Frieder Klein [a], Rebecca Kuehn [o], Kuan-Yu Lin [p], C. Johan Lissenberg [q], Haiyang Liu [r], Ethan L. Lopes [s], Toshio Nozaka [t], William Osborne [e], Andrew J. Parsons [u], Vamdev Pathak [v], Jessica Rodgers [a], Jeffrey S. Seewald [a], Kenneth W. Sims [n], Gordon Southam [w], Sean Sylva [a], Fengping Wang [x]

[a] Depts. of Geol. and Geophys. and Marine Chem. and Geochem., Woods Hole Oceanographic Institution, Woods Hole MA, USA
[b] Global Undersea Research Unit, University of Alaska Fairbanks, Moss Landing CA, USA
[c] Dept. Earth and Planetary Sciences, University of California, Santa Cruz, CA, USA
[d] Dept. Earth and Environmental Sciences, University of Iowa, Iowa City IA, USA
[e] School of Earth and Environment, University of Leeds, Leeds, the United Kingdom of Great Britain and Northern Ireland
[f] School of Molecular Sciences, Arizona State University, Phoenix AZ, USA
[g] School of Biological Sciences, University of Utah, Salt Lake City UT, USA
[h] International Ocean Discovery Program, Texas A&M University, College Station TX, USA
[i] Japan Agency for Marine-Earth Science and Technology, Yokohama, Japan
[j] Instituto Andaluz de Ciencias de la Tierra (IACT), CSIC, Armilla, Granada, Spain
[k] ISTO, UMR 7327, Univ Orleans, CNRS, BRGM, OSUC F-45071 Orléans, France
[l] School of Biological, Environmental, and Earth Sciences, University of Southern Mississippi, Hattiesburg MS, USA
[m] Geosciences Montpellier, CNRS, University of Montpellier, Montpellier, France
[n] Depart. of Geology and Geophysics, University of Wyoming, Laramie WY, USA
[o] Institute of Geosciences and Geography, Martin-Luther-University Halle-Wittenberg, Halle, Germany
[p] National Museum of Natural History, Smithsonian Institution, Washington, DC, USA
[q] School of Earth and Environmental Sciences, Cardiff University, Cardiff, the United Kingdom of Great Britain and Northern Ireland
[r] Center of Deep Sea Research, Institute of Oceanology, Chinese Acad. Sciences, Qingdao, China
[s] Dept. of Geophysics, Stanford University, Stanford CA, USA
[t] Dept. Earth Sciences, Okayama University, Okayama, Japan
[u] School of Geography, Earth and Environmental Sciences, University of Plymouth, Plymouth, the United Kingdom of Great Britain and Northern Ireland
[v] Dept. Geology, Central University of Punjab, Bathinda, India
[w] School of the Environment and Sustainable Minerals Institute, University of Queensland, St. Lucia, QLD, Australia
[x] Key Laboratory of Polar Ecosystem and Climate Change, Ministry of Education, and School of Oceanography, Shanghai Jiao Tong University, Shanghai 200030, China

ARTICLE INFO

Associate editor: Benjamin Tutolo

Keywords:
Serpentinization
Hydrogen
Methane
Abiotic organic carbon

ABSTRACT

Water that flows through permeable ultramafic rocks produces high abundances of molecular hydrogen (H_2), methane (CH_4), and other small organic molecules. Such products can fuel life in the rocky subseafloor, be extracted for energy, and may have played a role in pre-biological chemical synthesis on early Earth or other planetary bodies. The International Ocean Discovery Program drilled a new 1268-m-deep borehole (U1601C) into serpentinized mantle with minor gabbroic rocks on the Atlantis Massif, ~800-m north of the Lost City hydrothermal field (30°N, Mid-Atlantic Ridge). Measured temperatures of the disturbed borehole reached 91.3 °C, and equilibrated temperatures of the deepest section are estimated to be between 110 – 140 °C. Water

* Corresponding author.
E-mail address: sqlang@whoi.edu (S.Q. Lang).

https://doi.org/10.1016/j.gca.2025.09.024
Received 24 February 2025; Accepted 17 September 2025
Available online 20 September 2025

Organic acids
Ocean worlds
Prebiotic precursors
Formation waters
International Ocean Discovery Program
Expedition 399
Site 1601

collected every ~ 5-m during drilling operations had H_2 concentrations that were regularly > 200 nM and spiked to > 10 μM at multiple depths. In these waters, carbon monoxide was only present in deeper, hotter sections, and potentially associated with gabbroic intrusions into the peridotite host. Open borehole fluids were sampled after drilling and samples recovered from the deepest portion contained elevated short-lived 222-Radon and strontium isotope ratios similar to Lost City fluids, pointing to the presence of *in situ* subseafloor formation waters that have equilibrated with the host rock. The deepest samples were actively degassing upon recovery and contained 740 ± 360 μM H_2, 340 ± 36 μM CH_4, and 25.5 μM ∑formate (= formate and formic acid). The shallowest fluids from the open borehole also contain micromolar H_2 and ∑formate concentrations, the presence of which cannot be attributed to the upward migration of the deeper, higher concentration fluids.

We interpret these data as reflecting two distinct and interconnected regimes of fluid flow and composition. Deep waters that are channelized along faults, lithologic contacts, and other high permeability pathways host high H_2 and CH_4 concentrations plus micromolar ∑formate that closely mirror the chemistry and isotopic signatures of LCHF vent fluids. Pervasive fluid flow permeates the mesh texture and microfracture network of the serpentinized peridotite and sustains H_2 and ∑formate even in the shallowest subseafloor intervals at mild temperatures. These findings demonstrate that both focused and pervasive fluid flow contribute to the transport, and potentially the generation, of reduced volatiles and C1 compounds within the Atlantis Massif.

1. Introduction

Seawater circulation through the Earth's lithosphere plays a fundamental role in shaping global biogeochemical cycles and influences the distribution of life (National Research Council, 1990). Across vast regions where ultramafic rocks are exposed at the seafloor, *i.e.,* throughout the Atlantic, Indian, and Arctic Oceans, serpentinization drives molecular hydrogen (H_2) production through water–rock alteration reactions (Charlou et al., 2010; Keir, 2010; Früh-Green et al., 2022; German et al., 2024). Geochemically generated H_2 fuels redox reactions that abiotically synthesizes organic molecules and sustain microbial ecosystems in the subseafloor (e.g., McCollom and Seewald, 2007; Schrenk et al., 2013). These processes provide analogs for potential life-supporting processes on icy moons like Europa or Enceladus (Glein et al., 2015; Spiers & Schmidt, 2023; Vance and Daswani, 2020), as well as for prebiotic chemistry on early Earth (Martin & Russell, 2007; Sleep et al., 2004). In addition to its planetary implications, serpentinization holds promise as a model for clean energy production, and the mechanisms leading to H_2 generation offers valuable insights into harnessing it as a sustainable energy source for human use (Osselin et al., 2022; Templeton et al., 2024).

However, H_2 alone does not dictate the potential for life or organic synthesis. Microbial metabolism and the abiotic formation of complex organic molecules also depend on environmental factors including carbon availability and temperature. The synthesis of complex organic matter – whether biotic or abiotic – requires simple carbon precursors like $\sum CO_2$ ($\sum CO_2 = H_2CO_3^* + HCO_3^- + CO_3^{2-}$) or other C1 molecules (McCollom and Seewald, 2007). Many low- to moderate-temperature serpentinizing environments host fluids with trace $\sum CO_2$ concentrations due to carbonate precipitation and the reduction of $\sum CO_2$ to methane (CH_4) or other organic compounds and reduced carbon (Schrenk et al., 2013; Lang & Brazelton, 2020). Temperature, in turn, exerts a fundamental control not only on H_2 production (e.g., McCollom and Bach, 2009; Klein et al., 2013), but also on microbial activity (e.g., Heberling et al., 2010; Orcutt et al., 2011) and carbon speciation (e.g., McCollom and Seewald, 2001; McCollom and Seewald, 2003; Seewald et al., 2006).

Central to many abiotic synthesis pathways is the initial reduction of $\sum CO_2$ to either carbon monoxide (CO) or ∑formate (= formate and formic acid) (Seewald et al., 2006; McCollom et al., 2010; He et al., 2021) through the inter-related reactions:

$$CO_{2,aq} + H_{2,(aq)} = HCOOH \quad (1)$$

$$CO_{2,aq} + H_{2,(aq)} = CO + H_2O \quad (2)$$

$$HCOOH = CO + H_2O \quad (3)$$

Both CO and ∑formate are critical intermediates for carbon–carbon bond formation, and experimental data suggests they can be more effective carbon sources than CO_2 (McCollom et al., 2010). ∑Formate can lead to the synthesis of amino acids, nucleic acids, and acetate (Miller, 1954; McCollom et al., 2010; Jin et al., 2021; Takabayashi et al., 2023) while hydrocarbon formation proceeds with CO (Taran et al., 2010; McCollom et al., 2010; He et al., 2021; Zhao et al., 2021). Methane (CH_4) is the most reduced single-carbon compound but may be largely inert in the abiotic formation of carbon–carbon bonds (McCollom et al., 2010). Thus, the distribution of $\sum CO_2$, CO, ∑formate, and CH_4 can ultimately shape both the potential for abiotic synthesis of complex organic molecules and the types of compounds that result.

These same compounds also influence the habitability of the ultramafic subseafloor. Microbial communities in the ultramafic subseafloor face challenges due to alkaline conditions and low $\sum CO_2$ availability, and may therefore rely on the availability of alternate carbon sources. (Schrenk et al., 2013; Lang & Brazelton, 2020). Indeed, chemoautotrophs including acetogens, methanogens, and sulfate-reducing bacteria fueled by H_2 and C1 compounds have been identified in various serpentinite-hosted ecosystems (Colman et al., 2022; Fones et al., 2021; Suzuki et al., 2024; Coleman et al., 2025), yet very low biomass levels have been observed in some serpentinized seafloor samples (Früh-Green et al., 2018; Motamedi et al., 2020; Goordial et al. 2021; Wee et al., 2021) and in ultrabasic groundwater associated with some continental serpentinite formations (Suzuki et al., 2013, 2024; Brazelton et al., 2017). Greater biomass is typically found in less alkaline fluids (Fones et al., 2019) and at surface expressions where subsurface fluids mix with more surface-exposed seawater or groundwater, potentially stimulating the development of biofilms (Schrenk et al., 2004; Templeton et al., 2021; Templeton & Caro, 2023). These broad microbiological trends are consistent with serpentinization providing important sources of potential energy in the form of H_2 and C1 compounds while creating physiological challenges with extreme levels of pH and availabilities of carbon and nutrients. Determinations of specific biogeochemical processes and ecological roles in the ultramafic subsurface, however, have been complicated by difficulties in the laboratory cultivation of relevant microorganisms (Miller et al., 2018; Quéméneur et al., 2019; Mei et al., 2022) and by the technical challenges of accessing pristine ultramafic subsurface environments that are isolated from surface interactions (Früh-Green et al., 2018).

The molecular suite of H_2, $\sum CO_2$, ∑formate, CH_4, and CO is not unique to Earth, and has been detected extensively in varying abundances throughout our solar system, including icy ocean worlds (Peter et al., 2024; Waite et al., 2009; Waite et al., 2006; Waite et al., 2017), interstellar medium (Ehrenfreund & Charnley, 2000; Irvine, 1998), comets and meteorites (Altwegg et al., 2017; Biver & Bockelée-Morvan, 2019; Goesmann et al., 2015; Huang et al., 2005; Glavin et al., 2025). Major questions remain, however, on the specific conditions that facilitate their formation, their expected relative abundances in different environments, and their co-occurrence with critical ingredients for the

emergence of life, such as a sustained energy source (Board et al., 2019). Understanding the natural distributions of this molecular suite will improve our ability to interpret chemical patterns as biosignatures and predict where life-supporting conditions may emerge.

Much of our knowledge of in situ subseafloor H_2 and C1 abundances is inferred from focused hydrothermal discharge (Charlou et al., 2010; Früh-Green et al., 2022; German et al., 2024) and laboratory experiments (e.g., McCollom et al., 2001; 2003; 2016; McCollom and Seewald, 2007; Allen and Seyfried, 2003). Hydrothermal fluids are rich in chemical information but represent point sources that integrate complex, heterogenous biotic and abiotic reactions that occur over long, tortuous fluid pathways within the subseafloor. Prior to discharge, cool, downwelling seawater is heated to 200–500 °C before cooling again during ascent to discharge at temperatures of 5 to 400 °C (e.g., Früh-Green et al., 2022). During upwelling to the seafloor, formation waters can lose heat via conduction to the surrounding rock matrix and undergo additional reactions that can substantially alter fluid composition (e.g., H_2, CH_4, CO_2, SO_4^{2-}, H_2S, nutrients, and trace metals) by biotic and abiotic processes (Von Damm and Lilley, 2004; Wankel et al., 2011; Lang et al., 2018; McDermott et al., 2020). Similarly, laboratory experiments, typically conducted with characteristic materials under well-constrained physical and chemical conditions, have elucidated reaction products and pathways, and provide important bounds for reaction conditions (e.g., McCollom and Seewald, 2007). However, such experiments cannot adequately replicate the complex, heterogeneous pathways through which seawater travels within the subseafloor.

The Lost City hydrothermal field (LCHF; 30°N, 42°N), located on the southern flank of the Atlantis Massif, is a model site for studying serpentinization processes. Discharging fluids have low-to-moderate temperatures (45 – 116 °C), are alkaline (pH 9–10.6) and are enriched in H_2, CH_4, ∑formate, and n-alkanes (Kelley et al., 2005; Lang et al., 2010; Proskurowski et al., 2008; Seyfried et al., 2015). Microbial activity in the subseafloor and chimneys of the LCHF lowers H_2 concentrations due to sulfate reduction and other metabolisms (e.g., Proskurowski et al., 2006; Lang et al., 2018; Aquino et al., 2022), contributes to the presence of CH_4 (Bradley & Summons, 2010), facilitates the equilibration of ∑CO_2 and formate (Lang et al., 2018; McGonigle et al., 2020), and increases acetate and amino acid concentrations (Lang et al., 2010; 2012). These transformations alter the abiotic subseafloor distributions of geochemical species, underscoring the need to unravel subsurface dynamics to illuminate the interplay of microbial and abiotic processes and pathways.

While H_2 from LCHF fluids is well documented, the extent of its distribution in the subseafloor is poorly constrained. It is unclear whether H_2 is primarily localized within permeable fractures that direct focused hydrothermal flow, or if it is more broadly distributed throughout the rocky subseafloor. The shallow subseafloor across the top of the Atlantis Massif has temperatures too low to facilitate rapid

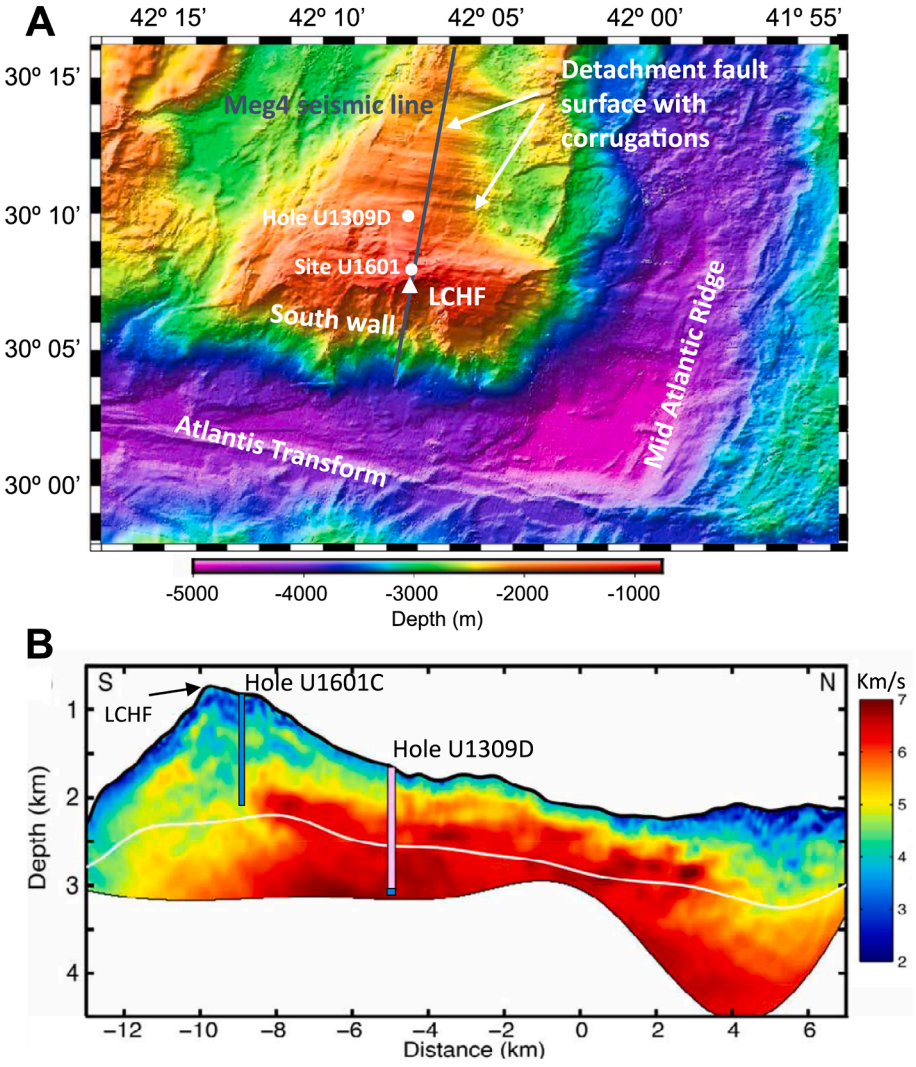

Fig. 1. (A) Bathymetric map of the Atlantis Massif indicating the location of Site U1601, Hole U1309D, and the Lost City hydrothermal field (LCHF); adapted from Früh-Green et al. (2017). (B) Seismic line Meg 4 with locations of the newly drilled Hole U1601C and Hole U1309D; adapted from Harding et al. (2016).

serpentinization and H_2 production, and yet it exports low concentrations of H_2 to the water column independent of the main hydrothermal field (e.g., Lang et al., 2021). Similarly, it remains unclear how deep $\sum CO_2$ and other C1 compounds extend into the subsurface and whether they are available for microbial or abiotic synthesis reactions.

Ocean drilling provides direct access to observe current subseafloor circulation of altered seawater by intersecting channelized flow within high permeability conduits, as well as water in host rock pore spaces. A new 1268-m-deep borehole (Hole U1601C; IODP Expedition 399) was drilled on the Atlantis Massif, approximately 800 m north of the LCHF,

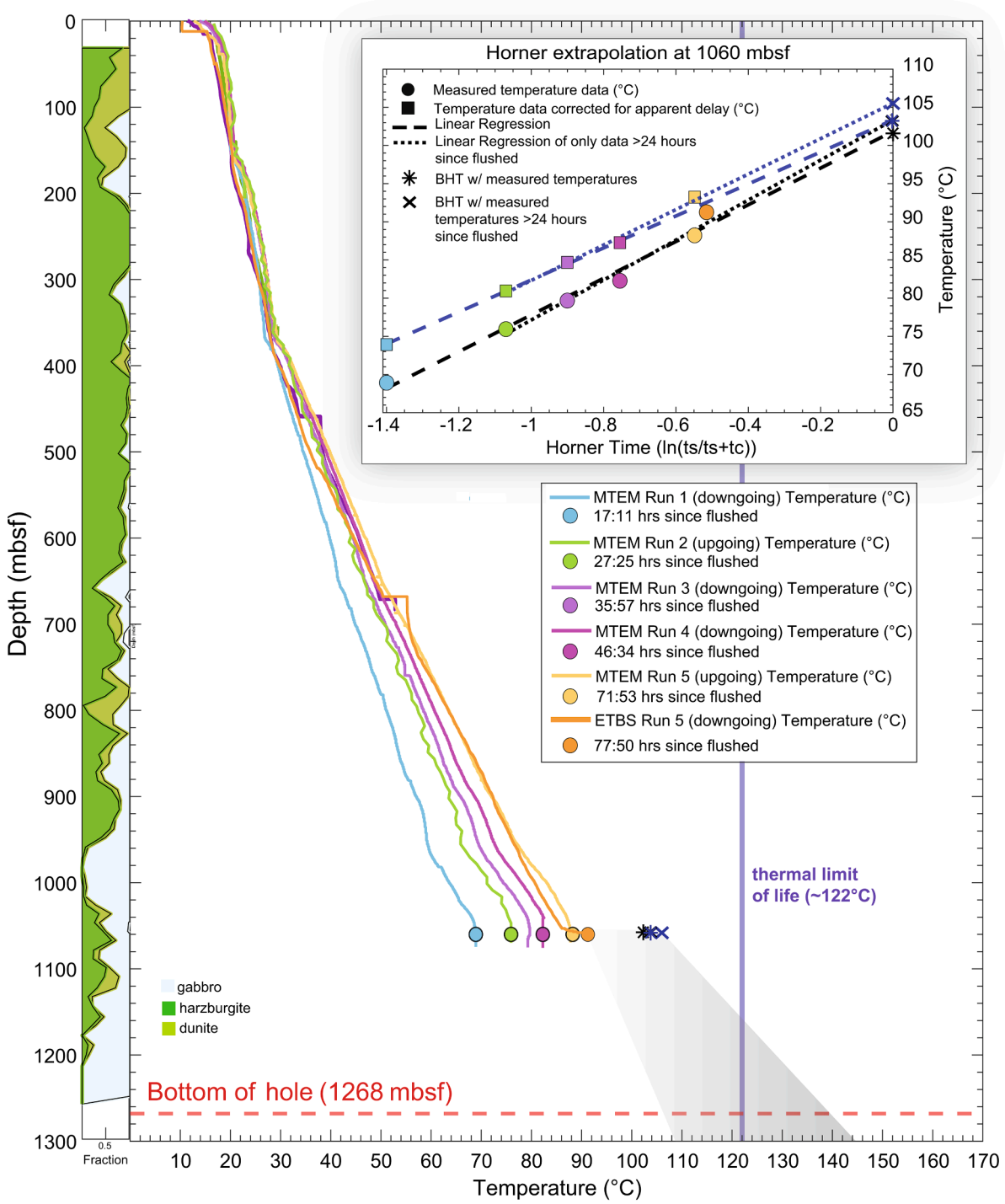

Fig. 2. Lithology and measured and estimated thermal profiles of six downhole runs in IODP Hole U1601C. Lithology of recovered rock types is a 20-m running average of harzburgite in dark green, dunite (including orthopyroxene-bearing dunite) in light green, and gabbro in blue. White represents no recovery. Five temperature profiles were measured by the Logging Equipment Head-Mud Temperature Log (LEH-MTEM) attached to the top of the logging tools, and one was measured by the Elevated Temperature Borehole Sonde (ETBS) during the final fluid sampling run. Measured Temperatures were collected ~ 19 – 80 hr after the hole was flushed with cool fresh water (and are therefore out of equilibrium with the formation). Inset in upper right corner shows a range of estimations of measured (circles) and calculated equilibrated (squares) bottom hole formation temperatures (BHT) at 1060 mbsf using the Horner method. Formation temperatures at the bottom of the hole (1268 mbsf) (shaded gray) were estimated based on extrapolations of linear regressions of the equilibrated thermal profile and the equilibrated thermal gradient observed in the nearby IODP Hole U1309D. See text for further details.

through primarily serpentinized mantle rocks that have been tectonically unroofed at the seafloor (Fig. 1) (Lissenberg et al., 2024; McCaig et al., 2024; Lang et al., 2025). By analyzing waters collected during drilling and subsequent borehole monitoring, we can trace downhole distributions of H_2 and C_1 species as they vary with depth, temperature, and lithology, offering new insight into the biogeochemical dynamics of ultramafic systems.

2. Geologic setting and major features of Hole U1601C

The Atlantis Massif is an oceanic core complex located at 30°N, approximately 15 km to the west of the Mid-Atlantic Ridge, and formed within the last 1.2 – 2 My (Escartín et al., 2022; Grimes et al., 2008). A detachment fault zone forms the surface of the Massif, which reaches a summit at a water depth of ~ 780 m (Schroeder and John, 2004; Karson et al., 2006). LCHF is situated south of the summit and consists of multiple large carbonate-brucite towers venting warm, alkaline fluids (Kelley et al., 2005). Several expeditions have visited the massif including four previous IODP expeditions (304, 305, 340 T and 357) (Blackman et al., 2011; 2014; Früh-Green et al., 2018), dredging and geological studies (Blackman and Collins, 2010; Blackman et al., 1998; Cann et al., 1997; Karson et al., 2006; Kelley et al., 2001) and fluid sampling efforts with submersibles and remotely operated vehicles (Kelley et al., 2005; Konn et al., 2009; McCollom et al., 2015; Lang et al., 2018).

IODP Hole U1309D was drilled 5 km north of the LCHF and penetrates largely gabbroic rocks to a depth of 1498 m below seafloor (mbsf; Fig. 1). In contrast, rocks recovered from the southern wall of the massif are dominantly serpentinized peridotite with minor gabbroic intrusions (Blackman et al., 1998; 2002; 2011; Cann et al., 1997). Seismic data indicates the gabbroic rocks at Hole U1309D extend to ~ 2.5 km below the seafloor (Fig. 1; Harding et al., 2016). During IODP Expedition 340 T (2012), Hole U1309D was revisited 7 years after drilling was completed and exhibited a nearly linear temperature profile below 750 mbsf, indicating a conductive thermal gradient in the lower portion of the hole (Blackman et al., 2014).

IODP Expedition 357 (2015) drilled a series of 17 shallow (<17 m) holes across the massif (Früh-Green et al., 2018). Cores recovered from the central sites contained diverse rock types including calcareous sediments, basalt, dolerite, and serpentinized harzburgite. Concentrations of H_2 were elevated to ~ 40 nM in the water column above these locations, suggesting that deeper drilling may encounter rocks undergoing active serpentinization (Früh Green et al., 2018; Lang et al., 2021).

In 2023, Hole U1601C was drilled adjacent to the central IODP Expedition 357 holes at the summit of the Atlantis Massif, and detailed information on its lithology, alteration minerology, and structural geology is reported in Lissenberg et al. (2024); McCaig et al. (2024); Lang et al. (2025). Here, we summarize important geologic features that could affect the chemical composition of formation waters. Rocks recovered from the borehole primarily consist of serpentinized mantle peridotite interleaved with gabbroic intrusions of variable thickness. Thin gabbroic layers are relatively common between ~ 120 – 195 mbsf, whereas the section between 200 and 640 mbsf is dominated by serpentinized harzburgite with only rare serpentinized dunite and altered gabbro (Fig. 2). The proportion of gabbroic rocks increased below 640 mbsf, and it was the dominant rock type below ~ 950 mbsf. The degree of serpentinization is generally extensive, from 80 to 90 % in recovered peridotites, with an interval of less extensive serpentinization (~40 %) at ~ 740 mbsf (Lissenberg et al., 2024). A systematic increase or decrease in the extent of serpentinization downhole is not apparent; instead, the extent of serpentinization varies on centimeter to decameter scales, and appears to be more pervasive closer to gabbroic intrusions (Lissenberg et al., 2024). Based on the distribution of alteration mineral assemblages and the concentration of uranium in recovered rocks, which is likely derived from oxic seawater, low-temperature weathering by oxic seawater is largely constrained to the upper ~ 200 mbsf (Lissenberg et al., 2024; Lang et al., 2025). Fractures and microfaults (mm-scale offsets) are commonly observed between 0 and 1000 mbsf in both mafic and ultramafic lithologies and rarely observed between 1000 and 1268 mbsf (Lang et al., 2025).

3. Materials and methods

3.1. Drilling and flushing operations

Drilling commenced at Hole U1601C on May 2, 2023 with five coring runs that deepened the hole to 1182.2 mbsf. Surface seawater was used as the drilling fluid, and sepiolite mud sweeps were pumped every ~ 10 m of coring, and at the end of each run, to clear debris from the Hole. Prior to wireline logging and water sampling, the hole was flushed with six times the open hole volume (353,500 L) of seawater then one and a half times the volume (87,500 L) of freshwater to improve resistivity contrast (Shipboard Scientific Party 1999; Blackman et al., 2006). After logging and fluid sampling, a final coring run deepened the Hole to a depth of 1267.8 mbsf.

3.2. Temperature measurements

Five wireline logging runs were carried out, each with a Schlumberger Logging Equipment Head-Mud Temperature tool (LEH-MTEM) and, on one lowering, the Elevated Temperature Borehole Sonde (ETBS) (Shipboard Scientific Party, 1998, 2000). The ETBS was also deployed in conjunction with borehole fluid sampling. The ETBS has a longer thermal response time than the logging sensor (LEH-MTEM), leading to the ETBS underestimating temperatures during deployment in zones of increasing temperature with depth. To combat this slow response, the ETBS was paused at 100 m intervals for 5 min for the sensor to equilibrate with the formation (Fig. S1, S2).

3.3. Collection of fluid and volatile samples

3.3.1. Bottom water sampling

Bottom seawater samples were collected about 10 m above the seafloor before drilling and during bit changes to characterize the water column geochemistry. A pair of 1.7 and 5 L Niskin bottles (General Oceanics) were attached to the Vibration Isolated Television (VIT) frame and connected in series to the release mechanism of a deep-water positioning beacon (Falmouth Scientific Inc.).

Samples that required collection without exposure to air were subsampled from the Niskin bottles into syringes via acid cleaned tubing and included aliquots for pH, alkalinity, shipboard geochemistry, and volatiles. The tubing was removed for the remainder of sampling during which water from the Niskin bottle flowed directly into the sample bottle.

Samples were aliquoted for multiple analyses depending on total volume and sample availability. A 60 mL aliquot was sampled using an HDPE acid washed syringe with a 0.45 μm filter for routine shipboard analyses: salinity, pH, alkalinity, chlorinity measurements, and spectrophotometric, ion chromatographic (IC) and inductively coupled plasma–atomic emission spectrometry (ICP-AES) analyses. The remaining water was aliquoted for shore-based analyses including strontium (acid washed HDPE, 4 °C) and chlorine (evacuated 2 mL Exetainer, room temperature). Aliquots for organic acids were collected in acid-soaked HDPE 60 mL bottles and stored at −20 °C. Remaining fluids from the Niskin bottles were transferred to large glass bottles that were first rinsed with 0.2 μm filtered Milli-Q water and autoclaved. These fluid samples were filtered through 0.2 μm Sterivex filter cartridges, and the filtrate was used for radium isotope measurements.

3.3.2. Borehole sampling with Kuster Flow-Through Samplers (KFTS)

Two mechanical clock-activated Kuster Flow-Through Samplers (KFTS), each with a 600 mL sample chamber, were deployed in series

with the ETBS on the coring line inside the drill pipe and in the open borehole. The two bottles were deployed four times for a total of eight samples. The sample names (e.g., "KFTS-3-675mbsf") reflects the type of sample (KFTS), the deployment number (e.g., "3" for the third deployment of the expedition), and the depth of the sample (e.g., 675mbsf).

Samples were collected from the bottles by gravity and by pulling fluid into syringes following the protocol from IODP Expedition 376 (de Ronde et al., 2019). Prior to deployment in Hole U1601C, the interior of the KFTS were scrubbed with phosphate-free soap (Decon) and rinsed with Milli-Q water. The interior was then wiped down with methanol, followed by rinsing with 10 % hydrochloric acid, 5 % bleach, and multiple rinses with Milli-Q water. Between the multiple deployments in Hole U1601C the interiors were rinsed with Milli-Q water. Sample aliquots were collected as described for the Niskin water column samples, though due to sample volume limitations not all samples could be collected at all depths. Two KFTS samplers did not close properly, leading to only partial recovery of the water samples (KFTS-4-675mbsf, KFTS-6-1065mbsf). Samples were analyzed shipboard for salinity, pH, alkalinity, chlorinity, IC, ICP-AES, radon isotopes, and dissolved gases (H_2, CO, CH_4, n-alkanes). Shore-based analyses included methane isotopes, organic acid concentrations, and isotopes of strontium.

3.3.3. Fluids recovered with cores

When cores were recovered, small amounts of fluid were trapped in the core catcher. From core U1601C-58R on, the fluid trapped on the lip of the core catcher was collected into a gas tight syringe. Due to volume constraints these samples were analyzed solely for H_2 and CO concentrations (n = 176).

3.4. Shipboard analytical procedures

3.4.1. Salinity, alkalinity, and pH

Salinity, alkalinity and pH were determined shipboard following the procedures in Gieskes et al. (1991). Salinity was measured using a Fisher temperature-compensated handheld refractometer (Fisher model: S66366). Fluid pH was measured with a combination of glass electrode standardized with pH 4, 7, and 10 buffers (±0.02 at 25 °C; National Institute of Standards and Technology [NIST] traceable). Alkalinity was determined by Gran titration with an autotitrator (Metrohm 794 basic Titrino) using 0.1 M HCl at 25 °C. The IAPSO standard seawater was used as check standard and analyzed at the beginning and end of the sample set for each site and after every 10 samples. Repeated measurements of IAPSO standard seawater alkalinity yielded a precision ~ 1.6 %, based on the analysis of five bottom seawater samples.

3.4.2. Chlorinity and dissolved inorganic carbon

Chlorinities were measured through titration using a Metrohm 785 DMP autotitrator and silver nitrate ($AgNO_3$) solution, which was calibrated against repeated titrations of an IAPSO standard.

A 100 µL sample aliquot was diluted with 30 mL of nitric acid (0.1 N HNO_3) solution and titrated with 0.015 N $AgNO_3$. IAPSO standard solutions interspersed with the unknowns yielded a precision of 0.4 %, based on the analysis of five bottom seawater samples.

Concentrations of total dissolved inorganic carbon (ΣCO_2) were determined for each sample from the total alkalinity, after accounting for the concentrations of other contributing species (Table 1):

$$A_T \text{ (or Alk)} = [HCO_3^-] + 2[CO_3^{2-}] + [B(OH)_4^-] + [HSiO_3^-] + [HPO_4^-] + 2[PO_4^{3-}] + [OH^-] \quad (4)$$

The concentrations of total phosphate were negligible and therefore ignored. The concentration of borate, $[B(OH_4^-)]$, was calculated from the total boron concentrations (B_T) based on the pK'a of 8.6 for the reaction in seawater (Dickson, 1990):

$$[B(OH)_3] + 2\,H_2O = [B(OH)_4^-] + H_3O^+ \quad (5)$$

3.4.3. Dissolved gas concentrations (H_2, CO, CH_4, n-alkanes)

The concentrations of dissolved gases were analyzed at sea. Hydrogen (H_2), carbon monoxide (CO), methane (CH_4), and n-alkane concentrations were determined by equilibrating the fluid with a headspace of helium.

For H_2 and CO, the headspace gas was injected into an Agilent G1530A gas chromatograph (GC) equipped with a Restek MolSieve 13 packed column (80/100 mesh, 6 ft, 2 mm ID) and a helium ionization detector at a constant temperature of 60 °C. The detection limit of the analysis was 3 nM.

For CH_4 and n-alkanes (ethene + ethane (C2), propene + propane (C3), i-butane (i-C4), n-butane (n-C4), i-pentane (i-C5), n-pentane (n-C5), i-hexane (i-C6), and n-hexane (n-C6)), the headspace gas was injected into an Agilent 7890 GC equipped with a flame ionization detector set at 250 °C and a HP-Molsieve PLOT column (60 m x 0.53 mm x 40 µm) at an initial temperature of 35 °C. After holding for 4 min., the oven was ramped at 25 °C min^{-1} to 200 °C and held for 5 min. Excess

Table 1
Measured geochemistry of 1601C borehole fluids collected by Kuster samplers. Upon recovery some sample bottles were leaking and exposed to atmosphere; these are denoted with a **. Temperatures are those measured on the KFTS assemblage at the time of sampling. Below detection is bdl and not measured is N.M.

Sample Name	Depth	Temp.	pH	Salinity	Alk.	Cl	B	Si	DIC[a]	$^{87}Sr/^{86}Sr$	^{222}Rn[b]	∑Formate	
	mbsf	(°C)		ppt	mM	mM	µM	µM	mM		dpm L^{-1}	µM	f_{fresh}[c]
KFTS-3-146mbsf	146	21.0	8.0	31	2.1	500	366	70	1.92	0.709161		5.0	0.11
KFTS-3-368mbsf	368	21.6	8.3	20	1.7	326	219	51	1.57	0.709069	N.M.	9.3	0.42
KFTS-4-465mbsf	465	37.9	8.4	8	1.4	150	87	43	1.35	0.709101	N.M.	bdl	0.73
KFTS-4-675mbsf **	675	52.9	8.0	11	1.2	193	108	19	1.19	N.M.	N.M.	N.M.	0.64
KFTS-6-675mbsf	675	55.2	8.1	10	0.7	180	80	55	0.60	0.708445	bdl	1.6	0.67
KFTS-5-970mbsf	970	79.5	7.8	19	0.7	332	177	135	0.52	0.707148	25 ± 15	10.9	0.39
KFTS-6-1065mbsf **	1065	91.2	7.9	19	0.6	318	179	107	0.51	0.707006	N.M.	N.M.	0.41
KFTS-5-1075mbsf	1075	88.1	8.4	20	0.5	367	180	36	0.36	0.706372	2 ± 2	25.5	0.32
399-U1601A-NB-#1 (Deep seawater, 839 m)		2.0	7.8	35	2.3	563	404	16	2.2	0.70917	bdl	bdl	
Surface seawater			8.1	37	2.4	593	436	6	2.3	0.709193	N.M.	bdl	
Fresh drill water			8.0	0	1.1	0.22	<5	78	1.1	N.M.	bdl	bdl	
Drilling mud			7.6	37	2.1	580	N. M.	N. M.	N.M.	N.M.	N.M.	bdl	
Endmember Lost City fluid, Beehive[d]	851	116	10.6			541	38	73.3	<0.002	0.7065		51.2	

[a] Calcuated from alkalinity.
[b] At time of measurement c. 33 h after collection; no counts related to radioactive decay of ^{219}Rn were detected for any sample.
[c] Fraction fresh (f_{fresh}) calculated as described in section 2.4.8.
[d] From Seyfried et al., 2015 (temp, pH, Cl, B, Si), Aquino et al., 2022 (Sr isotopes), and Lang et al., 2024 (∑formate).

extracted headspace was injected into evacuated vacutainers (Labco) and stored at room temperature.

3.4.4. Dissolved Radon (Rn) isotopes

The Rn isotope content of fluids was determined with a Durridge Rad7 radon detector. This instrument was factory calibrated about a month before the expedition. This calibration was adjusted based on an analysis of ^{222}Rn from an equilibrated ^{226}Ra standard solution.

The Rad7 circulates air in a closed system through solutions in a 250 mL bottle. We used 225 mL of solution to prevent its loss during bubbling. The air from the sample is first sent through a Drierite-filled column to remove moisture before it circulates into the Rad7. The circulating air contains Rn removed from the solution. Within the Rad7 the Rn decays to short-lived Po daughters depending on isotope. These decays are measured, distinguished by energy. Multiple analyses are needed to determine initial Rn isotope abundances and evolution curves. The first analysis ideally occurs as soon after sample collection as possible. To check for ingrowth of ^{222}Rn by the decay of ^{226}Ra, most solutions were analyzed at least once more several days later. Background seawater was transferred directly from the Niskin container for analysis. Due to limited availability of KFTS borehole fluid samples, the Rn isotope analyses were conducted on the filtrate collected from filtering the samples through a 0.2 μm Sterivex filter cartridge, intended for future DNA sequencing analyses.

3.5. Shore-based analytical procedures

3.5.1. Methane isotopes

The stable carbon and hydrogen isotope compositions of CH_4 were quantified on a Finnigan DeltaPlus mass spectrometer interfaced to an Agilent 6890 gas chromatograph through a GC-C-II interface at the Woods Hole Oceanographic Institution (WHOI). The furnace was held at 950 °C for combustion during carbon isotope analysis and 1450 °C for pyrolysis during hydrogen isotope analysis. The analytical error based on reproducibility of external standards and the samples was ± 0.7 ‰ for δ^{13}C with the exception of KFTS-5-1075mbsf, which had poor reproducibility leading to an error of 1.9 ‰. The δ^{2}H data had an analytical error of 3.2 ‰ or better for all samples. Three samples were combined to obtain sufficient carbon for the analysis of the radiocarbon content ($F^{14}C$) of CH_4 at the National Ocean Sciences Accelerator Mass Spectrometry (NOSAMS) facility. Based on the amount of extracted methane, the majority of the sample was from KFTS-5–970 mbsf (96 %), with only minor contributions from KFTS-5-1075mbsf (3 %), and KFTS-6-1065mbsf (2 %).

3.5.2. Organic acid concentrations

Organic acid concentrations (formate, acetate, propionate, butyrate, lactate) were analyzed by the method of Albert and Martens (1997) at WHOI. Samples were derivatized with 2-Nitrophenylhydrazine hydrochloride and 1-(3-Dimethylaminopropyl)-3-ethylcarbodiimide hydrochloride and analyzed on a Thermo Ultimate 3000 UHPLC equipped with a Thermo Scientific Acclaim Organic Acid silica column (P/N 070086, 3.0x150 mm, 3.0 μm diameter). Compounds were detected at 400 nm with a UV/Vis detector. The detection limit was 0.5 μM for each compound.

3.5.3. Isotopes of Sr in the fluids and gabbros

Untreated and unspiked fluid samples were analyzed for strontium (Sr) isotope ratios at the University of Leeds. Fluid samples were first centrifuged, and 1 mL aliquots were dried in 15 mL Teflon jars on a hot plate and subsequently re-dissolved in ultrapure HNO_3 and processed by conventional ion-exchange chromatography using Eichrom's Sr Spec resin. The gabbro powders (both altered and unaltered) were repeatedly ultrasonicated and washed with distilled Milli-Q H_2O and then digested in 15 mL Teflon vials via standard silicate digestion procedure using HF: NO_3-HNO_3-HCl steps and UpA grade acids. Following Sr purification, aliquots of all fluid and rock samples were loaded onto a $TaCl_5$ layer that was pre-deposited at low (<0.6 A) current on a previously outgassed pure tungsten (W) metal filaments. Filaments were measured on a Thermo-Fisher Triton series multi-collector thermal ionization mass spectrometer running in static mode. The instrumental mass fractionation was corrected by normalizing results to $^{86}Sr/^{88}Sr = 0.1194$. Instrument errors for determinations of $^{87}Sr/^{86}Sr$ ratios are reported as 2σ. Strontium isotope compositions were adjusted to NBS SRM 987 value of 0.710248 (Thirlwall, 1991). External precision (2σ) for Sr isotopic ratios from successive replicate measurements of standards (NBS Std. 987 and USGS Stnds. BHVO-2 and AGV-2) was better than 25 ppm in respect to the values for the same standards reported in the literature (Weis et al., 2006). The total chemistry blanks for Sr were negligible (< 300 pg) when compared with the Sr concentrations of the rocks and fluids.

3.5.4. Carbon speciation

The equilibration of $\sum CO_2$, formic acid (HCOOH), formate ($HCOO^-$), and $CO_{(aq)}$ were determined by the conventions in McCollom and Seewald (2003) and Seewald et al., (2006). Equilibrium reactions for Eqs. (1)–(3) were determined by calculating the equilibrium constant (K_{eq}):

$$K_{eq} = (a_{products})/(a_{reactants}) \quad (6)$$

where $a_{product}$ and $a_{reactants}$ are the activities of the products and reactants of the reaction, respectively. The K_{eq} value for each reaction was calculated using the SUPCRT92 software (Johnson et al., 1992) with additional data from Shock (1995) at a pressure of at 250 bars. Activity coefficients were calculated for a fluid with a composition similar to seawater ionic strength at 25 °C, specifically 1 for uncharged, 0.6 and 0.3 for singly and doubly charged ions respectively, and 1 for neutral species. This approximation is valid given the minimal variation in ionic strength under these relatively low-temperature conditions.

3.5.5. Fluid compositions without freshwater component

The KFTS samples were a mixture of the freshwater used to flush the borehole prior to logging and one or more water sources with a salinity higher than that of freshwater. The concentration of Cl^- was used to determine the chemistry of the higher salinity waters in the absence of the freshwater component, with the relationship:

$$f_{fresh} = 1 - \frac{[Cl]_{sample} - [Cl]_{fresh}}{[Cl]_{hsw} - [Cl]_{fresh}} \quad (7)$$

where $[Cl]_{sample}$, $[Cl]_{fresh}$, and $[Cl]_{hsw}$ are the concentrations of Cl in the sample, the freshwater, and the higher salinity water, respectively, and f_{fresh} is the fraction of the sample due to freshwater. Based on the Sr isotope data (see Section 4.4.1), samples from depths < 500 mbsf are most similar to deep seawater, with a $[Cl]_{hsw}$ of 563 mM, while samples from > 500 mbsf are more similar to Lost City fluids, which have a $[Cl]_{hsw}$ of 541 mM (Seyfried et al., 2015).

The composition of the higher salinity waters without the contribution from the freshwater component was then calculated:

$$[X]_{hsw} = \frac{[X]_{sample} - ([X]_{fresh} \bullet f_{fresh})}{1 - f_{fresh}} \quad (8)$$

where [X] is the concentration of the chemical species of interest.

4. Results

4.1. Temperature

Thermal profiles were measured after the borehole was drilled to 1182 mbsf and flushed with seawater and then freshwater to improve wireline logging results (Table S1). Temperatures were measured from the seafloor to 1060 mbsf. Flushing during and after drilling caused the measured borehole temperatures to be out of equilibrium with the

formation. Therefore, all recorded temperatures in Hole U1601C are a minimum relative to pre-drilling conditions.

Measured temperatures increased with time over five logging runs and four KFTS runs, with a maximum recorded temperature of 91.3 °C at 1060 mbsf (Fig. 2, Table S2; S3). All measured temperatures had an apparent delay in the thermal response, most clearly demonstrated by an increase of > 5°C when the ETBS tool was held for 5 min every ~ 100 m (Fig. S1). Although these stops were performed only with the ETBS tool, data from the first logging run, which included both ETBS and LEH-MTEM tools, showed a notable sensor lag in the LEH-MTEM as well, particularly below ~ 600 mbsf (Fig. S2). These temperature lags were likely due to a delayed sensor response time, but local convection at the bottom of the hole cannot be ruled out (Allis et al., 2018).

To estimate the temperature at the bottom of the borehole, we applied the Horner method (*i.e.,* constant line source method; Bullard 1947; Dowdle and Cobb 1975; Allis et al., 2018). LEH-MTEM profiles from the downgoing logging runs 1, 3, and 4, and the upgoing logging runs 2 and 5 and ETBS profile from the final downgoing KFTS run were selected for subsequent processing due to their higher quality. Measured temperatures are plotted against dimensionless time:

$$t_{Horner} = \ln\left(t_s/(t_s + t_c)\right) \quad (9)$$

where t_c is the circulation time of water in the borehole and t_s is the shut-in time (*i.e.*, the time since circulation has stopped). Extrapolation of the linear regression yielded estimated formation temperatures at the Y-intercept of the semi-log plot.

We also estimated the formation temperature at the deepest measured point. Water was circulated at 1060 mbsf for approximately 66 h (t_c). Six measurements at this depth were taken at various times after flushing ended (t_s) (~17–78 h) (Fig. 2). An extrapolated temperature at the bottom of the borehole was calculated from the measured temperatures. In addition, the corrected temperatures (T_c) were also determined to account for the apparent delay in thermal response using the equation:

$$T_c = T + c \quad (10)$$

where T is the measured temperature and c is the correction factor. A correction value of c = 4.25 °C was used at 1060 mbsf based on the observed temperature increase during a stop in ETBS run 5 at this depth (Fig. 2).

The linear regressions of temperature with depth were first fit using all the data. The Horner method has been shown to underestimate formation temperatures at early shut-in times (<24 h), and estimates are often more accurate when early measurements are omitted (Wang et al., 2019; Espinosa-Paredes et al., 2003; Drury, 1984). We therefore also calculated the regressions using only the data collected > 24 hr after circulation ended. At 1060 mbsf, estimated equilibrated temperatures ranged from ~ 101° – 105 °C.

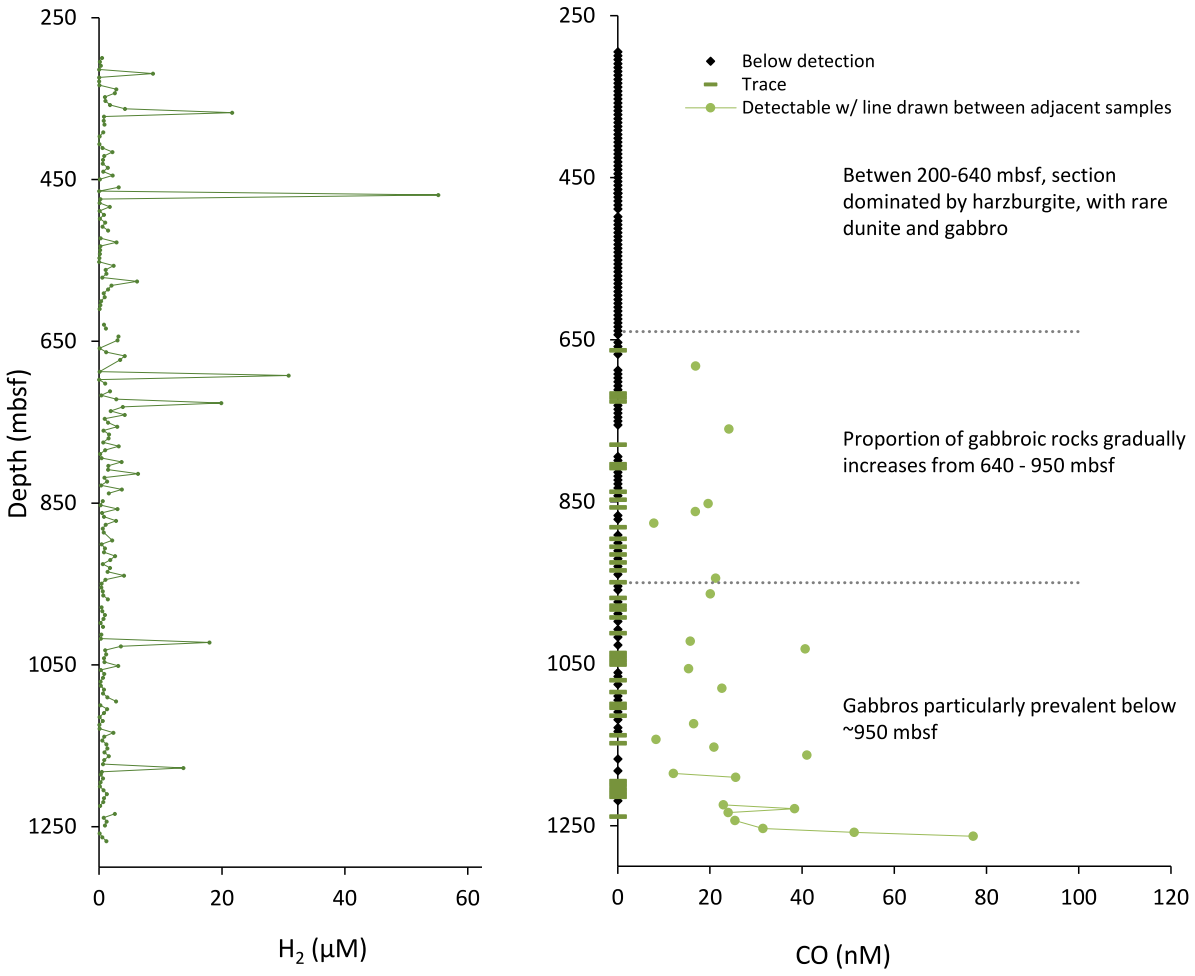

Fig. 3. H_2 and CO concentrations from core catcher fluid samples. H_2 concentrations are highly variable and do not align with physical measurements (e.g., porosity, alteration, etc.), nor with drilling conditions such as weight on bit or rate of penetration. H_2 is particularly sensitive to loss upon exposure to air, which may contribute to the observed variability. CO concentrations start increasing in the zone where the percentage of gabbroic rocks increase (640 mbsf) and reach the highest concentrations at depths where gabbroic rocks are particularly prevalent (>950 mbsf).

Drilling continued after the logging and fluid sampling runs that generated these temperature records. Given the final depth of Hole U1601C (1268 mbsf), we estimated the possible range of formation temperatures at the full depth based on extrapolations of (i) linear regressions of the estimated equilibrated formation thermal profile and (ii) the conductive thermal gradient from nearby IODP Hole U1309D where equilibrated temperatures have been measured (Blackman et al., 2014). At 1268 mbsf in Hole U1601C, temperatures were conservatively estimated to be ~ 110 – 140 °C. This extrapolation assumed similar heat flow behavior between the two boreholes, and did not account for potential differences due to thermal conductivity variations or convective flow.

4.2. Volatile abundances in core catcher fluids

The small volumes of fluid recovered with each 5-m core during drilling contained elevated H_2 and, in the deepest samples, $CO_{(aq)}$ (Fig. 3, Table S5). Concentrations of H_2 in core catcher samples were regularly > 200 nM and spiked to > 10 μM at multiple depths (Fig. 3, Table S5). The $CO_{(aq)}$ abundances were below the limit of quantification (LOQ; 5–10 nM depending on sample volume) in the uppermost portion of the borehole (Fig. 3, Table S5). Trace amounts of $CO_{(aq)}$ were present but below the LOQ at depths to 663 mbsf. Below this depth concentrations were quantifiable intermittently. Below 1224 mbsf, $CO_{(aq)}$ was quantifiable in all but one sample (23 – 77 nM; n = 8). For both H_2 and $CO_{(aq)}$, reported concentrations represent minimum values, as the samples were exposed to the atmosphere prior to analysis and likely incorporated some seawater used as drilling fluid.

4.3. Analyses of KFTS samples from open borehole

A total of 8 large volume (600 mL) KFTS samples were collected from the open borehole. We report here the results of shipboard and shore-based analyses that directly inform our interpretations of H_2 and C1 compound distributions (Table 1; Table 2; Fig. 5).

4.3.1. Salinity and Chlorinity of KFTS samples

Recovered borehole water samples had salinities from 8 to 31 per mil, with the lowest salinity sample from the mid-depth of 465 mbsf. Concentrations of chloride (Cl^-) had a similar distribution, with the highest Cl^- concentrations in the shallowest (146 mbsf, 500 mM) and deepest (1075 mbsf, 367 mM) samples. The freshwater flush had a low salinity (0 per mil) and chlorinity (0.22 mM). Surface seawater was slightly more saline and had higher chlorinity (37 ppt, 593 mM) than seawater collected from a water column depth of 839 m, approximately 5 m above the borehole (35 ppt, 563 mM) (Table 1).

Table 2
Measured H_2 and CH_4 concentrations and isotopes of CH_4 and DIC from 1601C borehole fluids collected by Kuster sampling. Samples with incomplete recovery identified with **.

Sample Name	Measured H_2	Measured CH_4	$\delta^{13}C$-CH_4	$\delta^{2}H$-CH_4	$\delta^{13}C$-DIC
	μM	μM	‰	‰	‰
KFTS-3-146mbsf	3	bdl			−1.1
KFTS-3-368mbsf	2	bdl			−3.6
KFTS-4-465mbsf	7	1			−6.3
KFTS-6-675mbsf	178 ± 6	42 ± 5	−13.1	−150	−7.6
KFTS-5-970mbsf	112	159	−15.3	−183	−7.1
KFTS-6-1065mbsf **	28 ± 8	23 ± 2.4	−12.6	−139	−6.7
KFTS-5-1075mbsf	742 ± 363	340 ± 36	−13.8	−125	−6.2
399-U1601A-NB-#1 (Deep seawater, 839 m)	bdl	bdl			0.21
Surface seawater	bdl	bdl			
Fresh drill water	bdl	bdl			
Drilling mud	bdl	bdl			
Endmember Lost City fluid, Beehive[a]	9600 ± 500	1100 ± 100	−12.6 to −9.3	−127 to −126	

[a] From Aquino et al., 2022 (H_2, CH_4 concentrations from 2018) and Proskurowski et al., 2008 (CH_4 isotopes from 2003).

4.3.2. Strontium isotopes of KFTS samples

The $^{87}Sr/^{86}Sr$ isotope ratios from the KFTS samplers ranged from 0.709161 to 0.706372 (Table 1; Fig. 4). Shallow borehole samples have $^{87}Sr/^{86}Sr$ isotope ratios similar to those in seawater (0.709193), while samples deeper than 700 mbsf are lower (0.706372–0.707148).

4.3.3. Radon isotopes of KFTS samples

Sample KFTS-5-970mbsf contained elevated activities of ^{222}Rn (26 ± 15 dpm L^{-1}) 33 h after collection (Table S4). Activities were below detection limits in this sample when remeasured 7 days later. Both values are minima since the sample degassed before the first measurement and bubbles grew on the sample bottle walls. These bubbles were lost before the second measurement. Activities of ^{222}Rn in other KTSF samples were at or below the detection limit of the Rad7 instrument, which is 2 dpm L^{-1}. Activities of all radon isotopes were below detection limits in a bottom seawater sample. ^{222}Rn is a noble gas radionuclide with a 3.82-day half-life that forms from the decay of longer-lived ^{226}Ra ($t_{1/2}$ = 1600 years). The lack of detection of ^{222}Rn during the second measurement of sample KFTS-5-970mbsf precludes significant activities of ^{226}Ra in this sample. However, the detection of rare counts related to the decays of ^{222}Rn and ^{220}Rn in other Kuster samples measured days to weeks after collection shows that ^{226}Ra and ^{224}Ra is present in these waters, but at activities of < 2 dpm L^{-1}. Activities of ^{219}Rn, and thus ^{223}Ra, were below detection limits for all fluid samples. This contrasts with fluids collected from LCHF vents, which had measured ^{223}Ra activities ranging from below detection limits to 97 dpm L^{-1} (Moore et al., 2021).

4.3.4. Volatiles (H_2, CH_4) of KFTS samples

H_2 was detectable in all KFTS samples from the open borehole and reached a high of 0.74 ± 0.36 mM (n = 3) in sample KFTS-5-1107mbsf (Table 2; Fig. 5). The large variability in replicates was due in part to active degassing of the sample during recovery, creating bubbles that contained high concentrations of H_2 and partially degassed liquids with

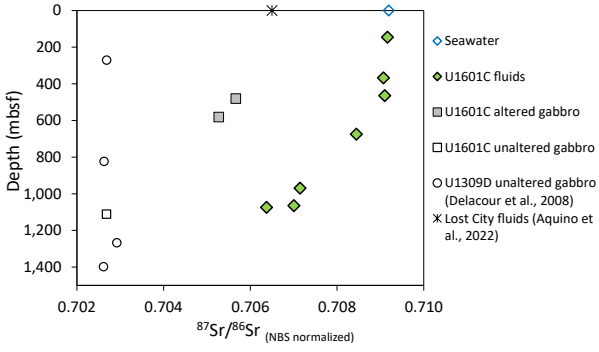

Fig. 4. $^{87}Sr/^{86}Sr$ isotope composition of seawater and borehole fluids (open and filled diamonds, respectively) contrasted against fresh and altered gabbros from U1601C (unfilled and filled squares, respectively). Also shown are literature values for unaltered gabbros from U1309D which are interpreted as reflecting the local source mantle (open circles: Delacour et al., 2008), and for LCHF vent fluid composition (star, Aquino et al., 2022). The Sr isotope composition of the borehole fluids approximates seawater values at depths < 600 mbsf but display relatively unradiogenic values that are comparable to LCHF vent fluid at depths > 600 mbsf. The intermediate Sr isotope ratios of the altered gabbros from U1601C highlights the interaction between advecting fluids and the fresh gabbro.

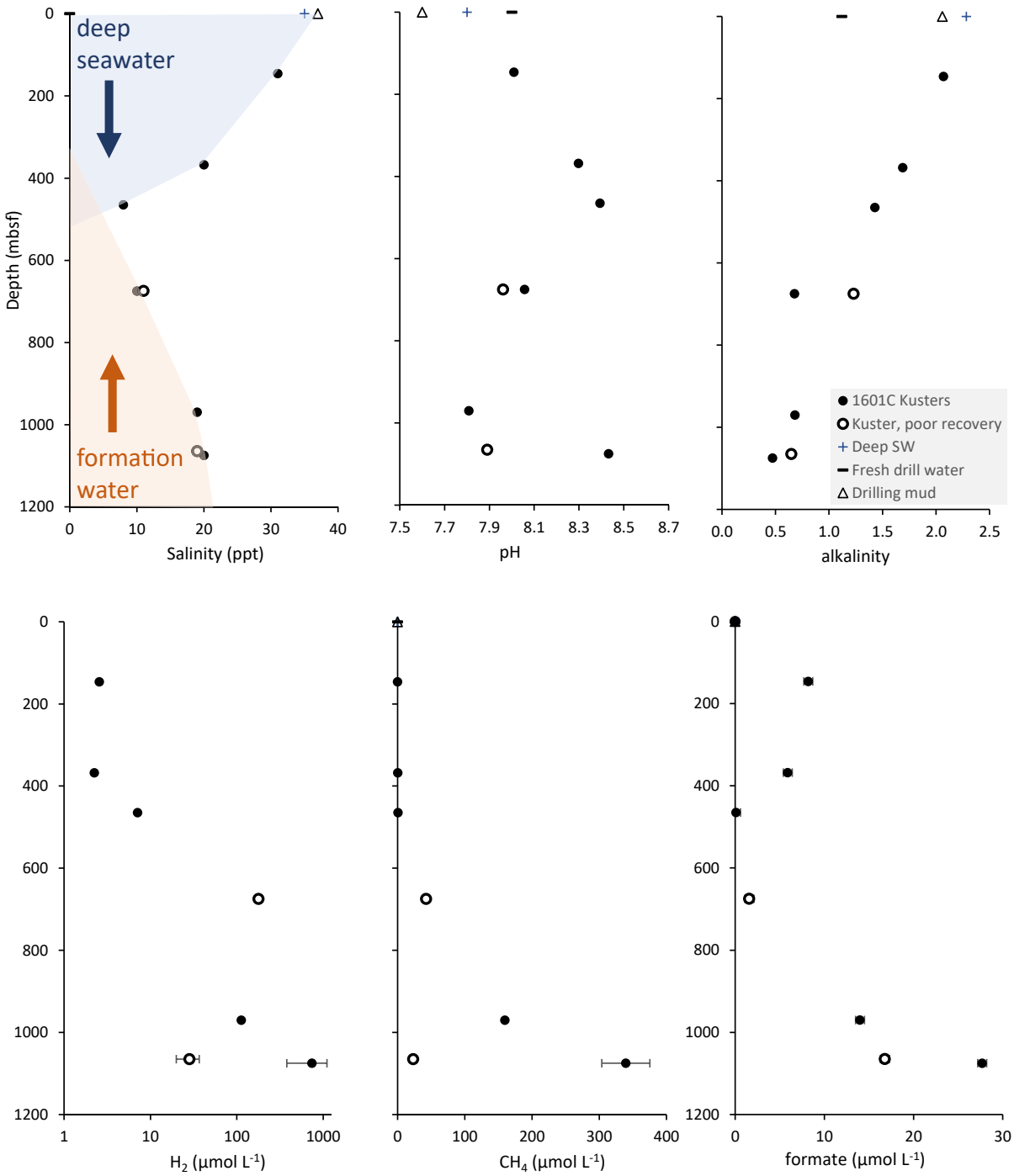

Fig. 5. Fluid geochemistry of KFTS borehole samples. The borehole was flushed with freshwater 78 hr before the first KFTS samples were collected. Replacement of freshwater with deep seawater and / or formation fluids has increased the salinity, but has yet to reach steady state conditions. Note log scale for H_2 concentrations. Error bars indicate standard deviation of replicate samples.

lower H_2.

Similar to H_2, concentrations of CH_4 increased with depth in the open borehole to a high of 0.34 ± 0.035 mM (n = 3; Table 2; Fig. 5). Unlike H_2, however, CH_4 was below detection in the shallowest samples. The effect of disturbing the hole was evident by higher CH_4 concentrations in sample KFTS-5-970mbsf (159 µM) than the following run of KFTS-6-675mbsf or KFTS-6-1065mbsf (22 – 46 µM). The $\delta^{13}C$ of CH_4 in the KFTS samples ranged from −15.3 to −12.6 ‰ and had δ^2H_{CH4} values of −183 to −125 ‰. The $F^{14}C$ of the CH_4 from three combined samples was 0.183 ± 0.002 (accession #OS-179443). N-alkanes (C2 - C6) were not detected.

4.3.5. *Dissolved inorganic carbon of KFTS samples*

The concentration of $\sum CO_2$ decreased down the borehole (Table 1). After correcting for the contribution from the freshwater flush, the deepest samples contained between 0 – 0.15 µM (Table 3). The freshwater flush contained 1.1 mM $\sum CO_2$, an order of magnitude higher than the formation waters (Table 1). Therefore, the isotopic composition of the measured $\sum CO_2$ (−7.1 to −6.2 ‰ in the deepest samples; Table 2) largely reflects the carbon carried with the freshwater flush in the deeper portions of the borehole.

Table 3
Calculated carbon and volatile content of high salinity water (HSW) captured with the Kuster bottles, after accounting for the freshwater component (see section 2.4.8). At depths < 500 mbsf, the HSW is inferred to have a Cl of deep seawater (563 mM). At depths > 500 mbsf, the HSW is inferred to have a Cl similar to Lost City fluids (541 mM; Seyfried et al., 2015). Below detection is bdl.

Sample Name	Depth	Temp.	DIC	Minimum H_2	Minimum CH_4	Formate
	mbsf	(°C)	mM	μM	μM	μM
KFTS-3-146mbsf	146	21	2.0	3	bdl	5.6
KFTS-3-368mbsf	368	22	1.9	4	bdl	16.1
KFTS-4-465mbsf	465	38	2.0	27	1.9	bdl
KFTS-6-675mbsf	675	55	0.00	536	126	5.0
KFTS-5-970mbsf	970	80	0.15	184	260	17.8
KFTS-5-1075mbsf	1075	88	0.01	1093	501	37.5
Deep seawater			2.2	bdl	bdl	bdl
Endmember Lost City fluid, Beehive[a]		116	< 0.1	9600 ± 500	1100 ± 100	51.2

[a] From Seyfried et al., 2015 (temperature), Aquino et al., 2022 (H_2, CH_4 concentrations from 2018), and Lang et al., 2024 (DIC, formate from 2018).

4.3.6. Organic acid concentrations of KFTS samples

Concentrations of ∑formate were highest in the shallowest and deepest borehole samples, and lowest in the low salinity sample KFTS-4-465mbsf. The concentrations of the deepest sample reached 25.5 μM and were calculated to be 37.5 μM in the pure formation water (Table 3). Concentrations of acetate, propionate, butyrate, and lactate were below detection limits of 0.5 μM in borehole samples.

5. Discussion

5.1. Temperature and preliminary insights into the thermal regime of U1601C

The rate of temperature increase over time was used to estimate the undisturbed (pre-drilling) temperature at the deepest measured depth of 1060 mbsf, resulting in a range from ~ 101 –105 °C (Fig. 2). Extrapolating the temperature profile to the full depth of the borehole (1268 mbsf) resulted in a conservative estimated temperatures of ~ 110 – 140 °C, bracketing the currently accepted upper thermal limit for life (122 °C) (Takai et al., 2008).

Deep borehole temperature profiles can provide insights into the heat flow and fluid convection that potentially supports the Lost City hydrothermal field. For example, nearby IODP Hole U1309D is 5 km to the North of Hole U1601C returned to thermal steady-state conditions (7) years after drilling (Blackman et al., 2014). Temperature profiles in this gabbro-dominated borehole indicated that it was cooled through slow downward advective seawater flow to depths of 750 mbsf, and controlled by a conductive thermal regime with a gradient of 113 °C km^{-1} below that depth (Blackman et al., 2014).

Based on the Hole U1309D thermal profile and the temperatures of Lost City fluids, geophysical modeling has suggested that maintaining hydrothermal circulation over the lifespan of the field would require formation waters to pass through high permeability regions in the southern portion of the Atlantis Massif, allowing heat to be mined from adjacent, low permeability rock that is largely conductively cooled (Titarenko & McCaig, 2016; Lowell, 2017). Hole U1309D was drilled into the low permeability region whereas Hole U1601C was drilled into the region predicted to have higher permeability.

Large deviations from the thermal profile of Hole U1309D would provide a clear indication of cooling from circulating fluids at Hole U1601C due to intersecting these higher permeability regions. At 1060 mbsf, thermally equilibrated Hole U1309D was 108 °C (Blackman et al., 2014), only slightly higher than our conservative estimates of undisturbed Hole U1601C temperatures at this depth (~101 – 105 °C). This small offset indicates that at these depths the thermal regime is primarily controlled by conductive cooling.

5.2. H_2 in core catcher fluids

Elevated H_2 concentrations are a defining feature of serpentinization systems (Moody, 1976; Neal and Stanger, 1983; Charlou et al., 2010; Früh-Green et al., 2022). H_2 is primarily generated through the reduction of water by Fe(II)-bearing minerals, a reaction predicted to proceed most efficiently at temperatures between 200 and 300° C (McCollom and Bach, 2009; Klein et al., 2013). In high temperature serpentinization-influenced hydrothermal systems, H_2 can reach 26 mmol/kg, substantially higher than mafic hosted systems (Charlou et al., 2010; Früh-Green et al., 2022). But H_2 is also detected at micro-molar and nano-molar concentrations in numerous cool ultramafic settings where high temperature circulation is not driving modern including waters circulating through continental ophiolites (e.g. Neal and Stanger, 1983; Abrajano et al., 1988; Etiope et al., 2011; Szponar et al., 2013; Leong et al., 2023) and across the top of the Atlantis Massif (Lang et al., 2021).

Core catcher fluids sampled at 5-m intervals offer the best representation of the formation waters occupying pore spaces in direct contact with the host rock at each depth (Fig. 3; Table S5). Across all measured depths, H_2 concentrations consistently exceeded 200 nM, and spiked to > 10 μM at multiple depths. These levels are significantly higher than those typically observed in sedimentary pore fluids, which are generally less than 5 nM and only occasionally reach 100 – 300 nM (Lin et al., 2012, and references therein). Thus, the elevated H_2 concentrations detected in the core catcher fluids demonstrate that it is present throughout the subseafloor at all sampled depths.

We considered whether artificial sources could cause elevated H_2 concentrations in core catcher fluids. For example, materials used to flush the borehole during drilling include surface seawater and drill mud that could contribute to collected fluid, but both have H_2 concentrations below the detection limit (Table 1). Mechano-radical reactions can also generate H_2 via seawater reactions with fresh surfaces of silicate and steel (Lefeuvre et al., 2024; Stevens & McKinley, 1995), with higher production associated with increased frictional work (Hirose et al., 2011). However, the highest H_2 concentrations were not associated with the highest weight on bit during drilling, nor the slowest rate of penetration, both indicators of higher frictional work (Fig. 6, Table S5). Drilling operations could also release H_2 and CH_4 known to be trapped in fluid inclusions present in rocks from the Atlantis Massif (e.g., Klein et al., 2019) but without quantitative data on the H_2 content trapped in fluid inclusions, the significance of this potential source cannot be well constrained (Supplementary Information). Despite the absence of quantitative constraints, the most likely explanation for the elevated H_2 concentrations in the core catcher fluids is that they captured formation waters while drilling.

We initially hypothesized that H_2 concentrations would correlate with physical parameters such as lithology or degree of serpentinization. However, at the scale of 5-m rock core sections, the highest H_2 concentrations are not consistently associated with the degree of serpentinization or with intervals composed of > 95 % purely peridotite or gabbro (Fig. 6; Table S5). The core catcher H_2 concentrations also show no consistent trend with depth or temperature, in contrast to the

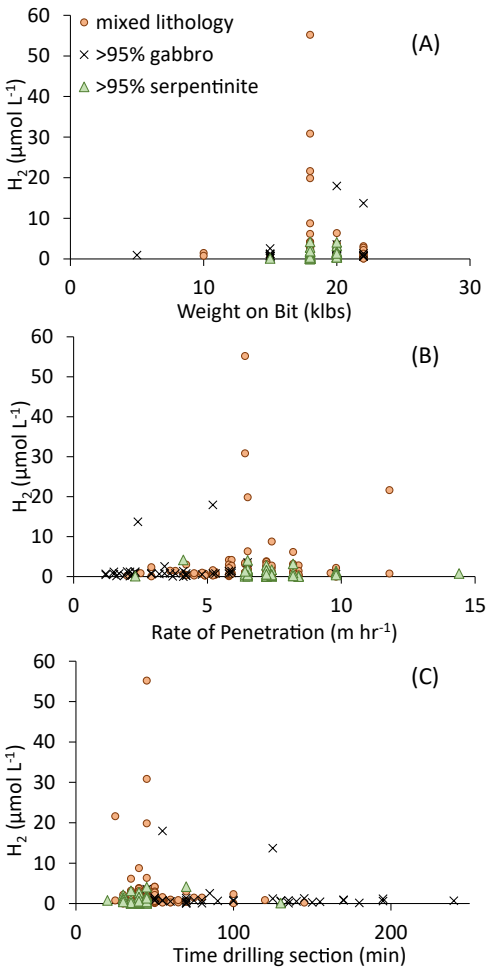

Fig. 6. Assessment of the potential for artificial H_2 generation due to increased mechanical work by comparison of (A) H_2 vs weight on bit (klbs) (B) H_2 vs. rate of penetration (m hr^{-1}) and (C) H_2 vs. time drilling section (min). The highest H_2 concentrations are associated with lithologies that are a combination of gabbro and serpentine, and are not associated with higher mechanical work induced by drilling.

systematic variations observed in fluids collected directly from the open borehole (see Section 4.4.2). Although the highest concentrations tend to occur in association with cores of mixed lithology, a Tukey's HSD test for multiple comparisons showed no statistical difference in the mean H_2 concentrations among the three lithologic groups (>95 % peridotite, >95 % gabbroic, mixed lithology; $p = 0.11$). Instead, the data indicate that H_2 is elevated at 10 s to 100 s of nanomolar concentrations throughout the rocky subseafloor at U1601C, across a large range of temperature conditions and in contact with all sampled lithologies. Occasional spikes to 10 s of µM are likely driven by localized heterogeneities that are not resolved at the 5-m sampling scale, or by larger scale hydrothermal transport processes that could not be captured by one set of fluid samples from a single borehole.

5.3. CO in core catcher fluids

While most fluids recovered with each 5-m core have CO abundances that are below detection limits, concentrations reach trace levels with increasing frequency in cores below 682 mbsf, and reach a high concentration of 77 nM in the deepest core (1263 mbsf; Table S5). The depths at which CO abundances start to increase roughly coincides with a change in core lithology at 650 mbsf, where the number and volume of gabbroic intrusions increase (Lissenberg et al., 2024; Lang et al., 2025). For comparison, fluids from the Lost City hydrothermal field do not contain detectable CO (Reeves et al., 2014).

Under equilibrium conditions, the abundance of CO is dependent on temperature, dissolved carbon content, and pH (Seewald et al., 2006; Fig. 7). In fluids with H_2 concentrations of 1 mM and 120 °C, CO formation will be favored at pHs < 6, though its concentrations will remain, as observed at Hole U1601C, substantially lower than $\sum CO_2$ or $\sum$formate (Fig. 7). At lower temperatures or lower H_2 abundances, the equilibrium concentration of CO decreases further relative to other C1 species (Fig. 7).

Detectable CO in deeper core catcher fluids is consistent with equilibration at the elevated temperature and potentially lower pH characteristic of the deeper borehole environment. Lower in situ pHs would arise from the substantial influence of gabbro in the deeper sections of the borehole, which would lower the fluid pH compared to a system buffered solely by peridotites (Moody, 1976; Seyfried and Bischoff, 1979; Palandri and Reed, 2004; Seyfried et al., 2015).

5.4. Insights from open borehole KFTS samples

5.4.1. Replacement of the freshwater flush by seawater and formation water

After drilling, water can enter the open borehole from downwelling seawater and from the surrounding rock formation. Since the borehole was flushed with freshwater prior to sampling with the large volume KFTS samplers, and these fluid sources have distinct geochemistry, their relative contributions to the borehole fluid samples can be calculated.

Samples had salinities and chlorinities lower than seawater, indicating that freshwater from flushing operations remained in the borehole to differing degrees. The samples with the lowest salinity were collected at a depth of 465 mbsf, while it above and below that depth (Table 1; Fig. 5). The higher salinities point to the replacement with deep seawater, formation water, or both. The high chlorinity in the deepest samples (> 600 mbsf) could be due to deep seawater that mixed heterogeneously during density-driven overturning of the borehole. Alternatively, formation waters that have equilibrated with the host rock could be flowing into the open borehole.

To distinguish these possibilities, we examined the strontium and radon isotopes of the water from the open boreholes. Shallow open borehole samples (<600 mbsf) have $^{87}Sr/^{86}Sr$ isotope ratios similar to seawater (0.7092) while deeper samples (>600 mbsf) display more unradiogenic values (0.7064–0.7072; Table 1; Fig. 4) consistent with significant amounts of formation fluids entering the borehole. The unradiogenic Sr isotopic values can be attributed to water–rock interaction with unaltered peridotite or, more likely, gabbroic rocks that have a higher Sr content (Ludwig et al., 2006; Delacour et al., 2008). Minimally altered gabbros from U1309D exhibit low $^{87}Sr/^{86}Sr$ ratios, averaging 0.702642 ± 0.000038 (n = 3), whereas extensively altered gabbros exposed on the southern wall have seawater-like compositions (0.70885–0.70918) (Delacour et al., 2008). Similarly, unaltered gabbros from U1601C have $^{87}Sr/^{86}Sr$ ratios (0.702683 ± 0.000011; Table S6) comparable to those from U1309D, while altered gabbros have elevated ratios (0.705467 ± 0.00279; Table S6) that reflect interaction with seawater or an evolved fluid. Substantially elevated $^{87}Sr/^{86}Sr$ isotopic compositions of altered gabbros relative to the local source mantle (Table 1; Table S6; Fig. 4) highlights the role of advecting fluids in modifying the initial compositions. The unradiogenic $^{87}Sr/^{86}Sr$ values in U1601C are similar to LCHF fluids from the central Beehive vent ($^{87}Sr/^{86}Sr = 0.7065$; Ludwig et al., 2006; Delacour et al., 2008), suggesting that both fluids are controlled by similar fluid-rock interactions in the deep basement of the massif.

A substantial contribution of formation fluids to borehole samples is also indicated by the elevated concentration of short-lived ^{222}Rn in sample KFTS-5-970mbsf shortly after collection, which requires a source from the decay of longer-lived ^{226}Ra. The ^{226}Ra was not present at detectable levels in the water itself based on the absence of ^{222}Rn 7 days after the initial analysis. Thus, the ^{222}Rn was sourced from the decay of

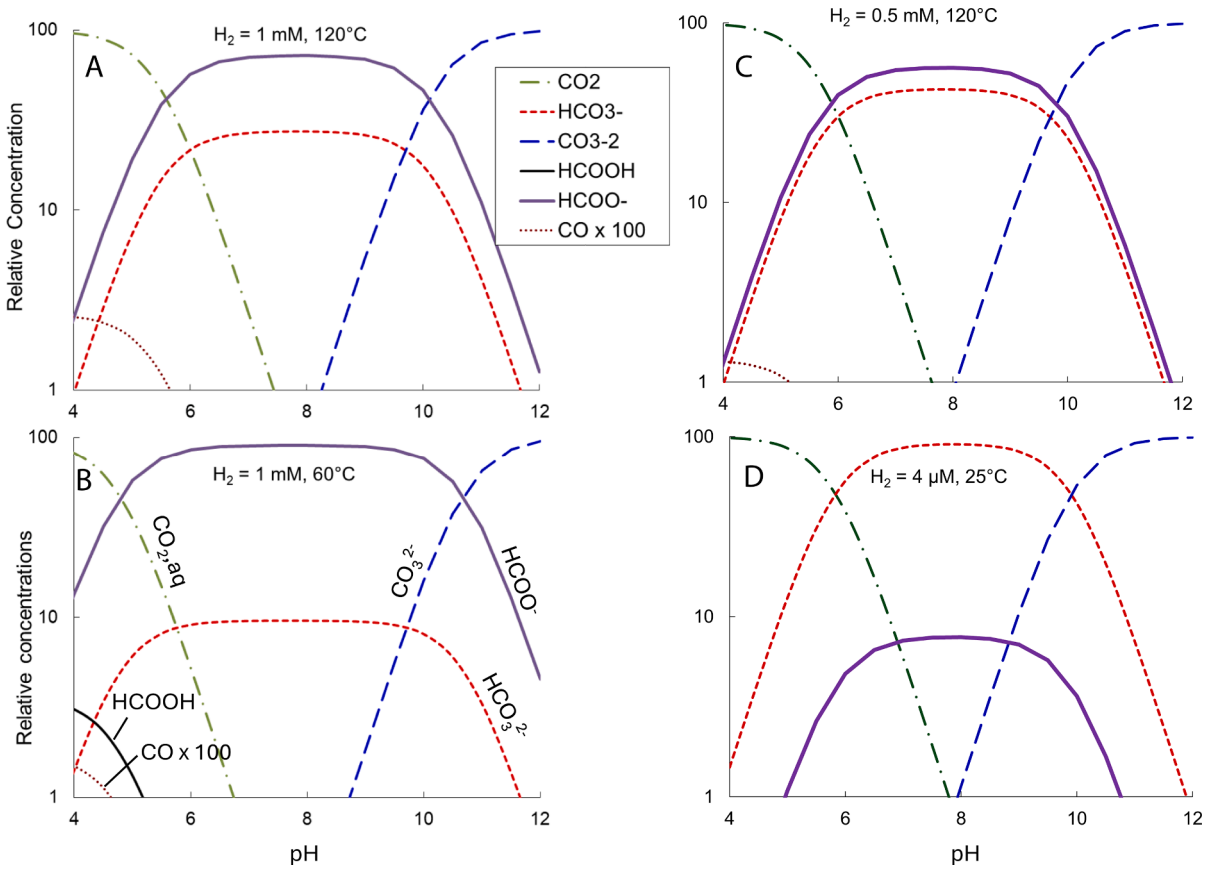

Fig. 7. Metastable equilibrium distribution vs pH among the single carbon compounds: $CO_{2(aq)}$, HCO_3^-, CO_3^{2-}, HCOOH, $HCOO^-$, and CO (x100) at 250 bars, after the conventions of McCollom and Seewald (2003) and Seewald et al., (2006) at (A) 120 °C, 1 mM H_2, (B) 60 °C, 1 mM H_2, (C) 120°C, 0.5 mM H_2 and (D) 25 °C, 4 µM H_2. Even at low temperatures and relatively low H_2 concentrations, some formate will be present at equilibrium conditions. The formation of CO is favored at higher temperatures and lower pH values.

^{226}Ra in materials (e.g., serpentinite, carbonate, clay; Spizzico, 2005; Moore et al., 2021) lining fluid-filled fractures, and transported with fluids that discharged into the borehole after it was flushed with freshwater. The lack of measurable ^{219}Rn in KFTS fluids from Hole U1601C implies longer residence times for these deeply sampled formation fluids compared with the < 3 yr residence times calculated for fluids vented from the LCHF (Moore et al., 2021).

5.4.2. *Hydrogen in open borehole samples*

The open borehole KFTS samples contained detectable H_2 in both the shallow and deep samples, reaching a maximum of 740 ± 360 µM at 1075 mbsf (Table 2). After accounting for the presence of the H_2-free freshwater, the minimum concentrations in these deepest waters are inferred to be 1090 µM H_2 (Table 3). For comparison, these concentrations are 5 – 28 % of the H_2 concentrations in Lost City hydrothermal fluids collected with gas-tight samplers in 2018 (2.6 – 13 mM (Aquino et al., 2022)).

H_2 present at low micro-molar concentrations in the shallowest open borehole samples could have been advected from deeper in the borehole or could have been sourced from local waters in equilibrium with the host rock, similar to the core catcher fluids. We compared H_2/CH_4 ratios to distinguish these possibilities (Fig. 8). The ratio is not altered by fluid transport or dilution with seawater but can be lowered by multiple biological processes. For example, in the subseafloor and chimneys at Lost City, H_2 concentrations are lowered due to microbial sulfate reduction, methanogenesis, and other metabolic activities (Proskurwoski et al., 2006; Lang et al., 2012; Brazelton et al., 2022). The subseafloor loss of H_2 and gain of CH_4 due to microbial activity is also frequently observed in the shallow subseafloor of hydrothermal systems

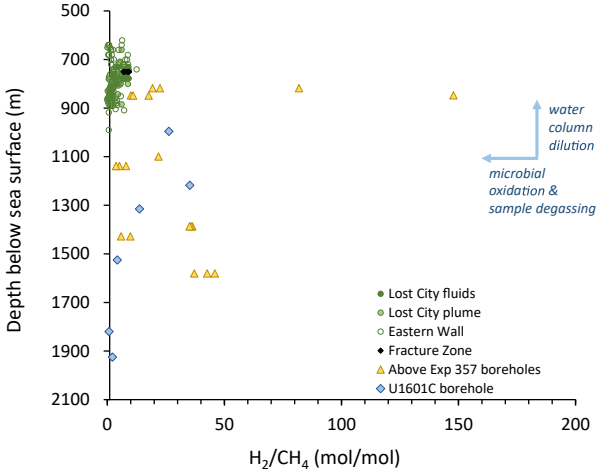

Fig. 8. Depth with respect to sea surface vs. H_2/CH_4 ratios of fluid samples. Dark green circles are fluids channeled through the LCHF chimneys (Proskurowski et al., 2008). Light green circles are from the LCHF plume, empty green circles are the eastern wall of the massif, black circles are from a tow-yo along the termination of the detachment fault, and yellow triangles are samples collected in the water column along the top of the massif (Lang et al., 2021). Samples from U1601C are plotted against depth below seafloor by adding the water column depth (850 m) to the depth below seafloor (blue diamonds). Samples across the top of the massif and those from U1601C have higher H_2/CH_4 ratios than those directly associated with the LCHF circulation pathway, suggesting a source distinct from the main field (see text).

(Von Damm and Lilley, 2004; Wankel et al., 2011). In oxic conditions, H_2 is consumed ~ 10x more rapidly than CH_4, which would also lower ratios (Kadko et al., 1990).

The H_2/CH_4 ratios of the shallow open borehole samples that are higher than those of the deep borehole samples and Lost City hydrothermal fluids suggest that they are a primary feature of the shallow fluids (Fig. 8), and do not reflect transport from deeper in the system. The most likely explanation is that the shallow fluids captured in the open borehole are distinct from those deep in the borehole. The ubiquitous, elevated levels of H_2 in the core catcher fluids further support its widespread and dispersed presence throughout this section of the massif. Moreover, the H_2/CH_4 ratios of shallow fluids from the open borehole are similar to water column samples collected above the Atlantis Massif on an earlier expedition (Fig. 8; Lang et al. 2021), indicating they are the likely source of H_2 actively exported from the shallow subseafloor into the overlying ocean.

Borehole temperatures at these shallower depths are well below the conditions where thermodynamic predictions suggest the highest H_2 concentrations (200 – 300 °C; Klein et al., 2013; McCollom & Bach, 2009). Nevertheless, the data reported here indicate that conditions leading to H_2 production or mobilization are active at lower temperatures in oceanic settings. Low temperature fluids influenced by serpentinization have long been recognized in continental settings (Barnes et al., 1967; Abrajano et al., 1988), and are now documented worldwide including in the Philippines, New Zealand, Turkey, California, Italy, New Caledonia, Canada, and Spain (see reviews in Etiope and Whiticar, 2019; Sherwood Lollar et al., 2024). The lateral spatial extent of diffuse H_2 outgassing can be considerable, spanning kilometers in regions such as the Oman ophiolite (Leong et al., 2021, 2023), and similarly observed across the summit of the Atlantis Massif (Lang et al., 2021). Laboratory experiments report H_2 production at low temperatures due to serpentinization (Neubeck et al., 2011; Okland et al., 2014; Mayhew et al., 2011), though some have questioned whether observed rates exceed background levels (McCollom and Donaldson, 2016). An alternative explanation is that H_2 in low temperature continental and marine systems is not newly generated, but rather remobilized from fluid inclusions that trapped gas during earlier, higher temperature conditions (Klein et al., 2019; Grozeva et al., 2020; Andreani et al., 2023). While our data cannot constrain these different mechanisms, our results show that low-temperature H_2 containing fluids are present throughout the top 1 km of serpentinized oceanic lithosphere, revealing its presence at a broad three-dimensional scale.

5.4.3. *Methane in open borehole samples*

In the open borehole KFTS samples, CH_4 concentrations increase downhole from below detection to a high of 340 ± 36 μM at 1075 mbsf (Table 2). After accounting for the presence of the volatile-free freshwater, the minimum concentrations in these deepest waters are 1090 μM H_2 and 500 μM CH_4 (Table 3). For comparison, these concentrations were 20 – 40 % of the CH_4 concentrations in Lost City hydrothermal fluids sampled with gas-tight samplers in 2018 (2.6 – 13 mM and 0.8 – 1.5 mM, respectively; (Aquino et al., 2022)).

Environments in which water reacts with ultramafic rocks have notably higher concentrations of CH_4 compared to mafic settings (e.g., Charlou et al., 2010; Früh-Green et al., 2022). Elevated H_2 concentrations produced as a result of serpentinization can drive the reduction of CO_2 to form CH_4, independent of biological processes (e.g., Charlou et al., 2002; McCollom and Seewald, 2007; Proskurowski et al., 2008). The ^{13}C, ^{14}C, and ^{2}H isotopes of CH_4 can be used to constrain synthesis pathways (Proskurowski et al., 2008; Etiope and Whiticar, 2019; Suda et al., 2022). More positive $\delta^{13}C$ values are generally associated with abiotic synthesis, and more negative values are associated with microbial methanogenesis or thermal degradation of organic matter (McCollom & Seewald, 2007).

Methane in Lost City fluids has been attributed to primarily abiotic processes based on stable and radiocarbon isotopes, with a potential minor contribution from microbial methanogenesis (Proskurowski et al., 2008; Bradley and Summons, 2010). Clumped isotopologue measurements of $\Delta^{13}CH_3D$ correspond to temperatures far hotter than the vent fluids themselves, suggesting the CH_4 formed or reequilibrated under hotter conditions (Wang et al., 2018; Labidi et al., 2020). The δ^2H values of CH_4 at Lost City reflect thermal equilibration, with cooler temperatures resulting in more negative values (Proskurowski et al., 2006). A mechanism that could account for formation temperatures higher than those encountered in the modern-day hydrothermal system is the contribution of methane-rich fluid inclusions trapped in olivine that are swept into hydrothermal fluids during circulation (e.g., Kelley and Früh-Green, 1999; McDermott et al., 2015; Klein et al., 2019).

The $\delta^{13}C$ of CH_4 in the KFTS samples ranged from −15.3 to −12.6 ‰, overlapping with but somewhat more negative than the CH_4 from LCHF (−12.6 to −9.3 ‰; Proskurowski et al., 2008). The KFTS samples have δ^2H_{CH4} values of −183 to −125 ‰, again overlapping but more negative than LCHF values (−141 to −99 ‰ (Proskurowski et al., 2006)), suggesting re-equilibration of this CH_4 at lower temperatures than the CH_4 in LCHF fluids.

These $\delta^{13}C$ and δ^2H isotope signatures point to a predominantly abiotic origin, similar to Lost City. However, radiocarbon analysis ($F^{14}C_{CH4} = 0.183 \pm 0.002$) requires an input of ~ 17 % modern carbon. Modern carbon was unlikely to be derived from subseafloor materials, as both Lost City fluids and the deep high salinity waters contain extremely low $\sum CO_2$ concentrations (Proskurowski et al., 2008; Lang et al., 2024; Table 1). Moreover, the $F^{14}C$ signatures of CH_4 from Lost City fluids were 0.0017 – 0.0062 (Proskurowski et al., 2008). The most plausible explanation is a small but detectable contribution of microbially produced methane generated after drilling, using drill-water $\sum CO_2$ that contains surface-seawater radiocarbon ($F^{14}C_{DIC} \approx 1.05$; Druffel et al., 2016). Because abiotic CH_4 synthesis is sluggish at temperatures < 250 °C (McCollom and Seewald, 2001; McCollom and Seewald, 2007), microbial methanogenesis is the likeliest mechanism for this modern component. Consistent with this interpretation, sample KFTS-5-970mbsf, which contributed 96 % of the combined sample, had $\delta^{13}C_{CH4}$ and δ^2H_{CH4} isotope values more negative than samples from other depths (Table 2), pointing to a small but discernible methanogenic overprint.

5.4.4. *∑Formate concentrations in open borehole samples*

The open borehole KFTS samples contained detectable ∑formate in both the shallow and deep samples, reaching a maximum of 37.5 μM in the pure formation fluid at 1075 mbsf (Table 1; Table 2). For comparison, the ∑formate of Lost City fluids has varied over time, with a maximum concentration of 158 μM in 2003 and 52 μM in 2018 (Lang et al., 2010; 2024).

∑formate is routinely detected at micro-molar to milli-molar concentrations in serpentinizing systems (Lang et al., 2010; McDermott et al., 2015; Kohl et al., 2016; Rempfert et al., 2017). Its abiotic formation was first predicted by thermodynamic models showing high H_2 activities favor its synthesis (Shock, 1992). Subsequent laboratory experiments confirmed these predictions, demonstrating rapid equilibration among ∑formate, $\sum CO_2$ and H_2, particularly at temperatures exceeding 250 °C (McCollom and Seewald, 2003). The first *in situ* detection of ∑formate occurred at LCHF, where isotopic evidence later reinforced its abiotic origin (Lang et al., 2010; Lang et al., 2018). Comparable micromolar-to millimolar concentrations, likewise attributed to abiotic synthesis, have since been reported at the Von Damm and Prony Bay vent fields (McDermott et al., 2015; Pisapia et al., 2017), the Mariana forearc subduction zone (Eickenbusch et al., 2019), Kidd Creek fracture waters (Sherwood Lollar et al., 2021), boreholes in the Oman ophiolite (Rempfert et al., 2017), and the Cedars serpentinizing springs (Kohl et al., 2016).

At the conditions of the bottom of Hole U1601C (H_2 = 1 mM; 120 °C), ∑formate is thermodynamically favored at equilibrium over $\sum CO_2$ and CO at pHs between 6 and 10 (Fig. 7a). The pH range of

favorable ∑formate speciation is similar at the lower temperatures representative of conditions in the mid-borehole environment (60 °C; Fig. 7b). The presence of elevated ∑formate in the deeper U1601C open borehole fluids is therefore consistent with previous observations that it will be favored at elevated H_2 concentrations (McCollom and Seewald, 2003; Seewald et al., 2006).

It is notable that ∑formate is also present in the shallowest open borehole samples (5.6 – 16.1 μM at depths of 148 and 386 mbsf; Table 3). Just below these depths (465 mbsf), the freshwater flush has been only minimally displaced by either downwelling seawater or upwelling formation waters (Section 4.2; Fig. 5), and ∑formate concentrations reach a minimum. The ∑formate in the shallower samples is therefore unlikely to be sourced from fluids rising from deeper in the borehole, suggesting *in situ* formation within the surrounding pore fluids.

Thermodynamic calculations support this interpretation. Under shallow-hole conditions (H_2 = 3 μM, 35 °C, pH 8), the expected equilibrium ratio of ∑formate/$\sum CO_2$ is 0.05, slightly higher than the calculated endmember ratios for the two shallowest samples (0.003 – 0.008; Table 3). These measured ratios are best matched at lower H_2 concentrations of 0.2–0.5 μM. In contrast, the elevated H_2 concentrations deeper in the borehole would yield equilibrium ∑formate/$\sum CO_2$ ratios near 16. Therefore, if the observed ∑formate/$\sum CO_2$ reflect equilibrium, they likely formed under low H_2 conditions consistent with those in the shallow borehole.

Taken together, the geochemical data and modeling indicate the ∑formate observed between 148 and 386 mbsf was generated locally, in fluids that have interacted with the surrounding shallow rock before being swept into the borehole, rather than being delivered from deeper horizons.

5.5. Fluid flow, volatile transport and storage

Our results reveal several distinct regimes of volatile and C1-compound distributions pointing to multiple fluid populations. Earlier studies have shown that fluid flow in ultramafic systems can occur either as localized channelized pathways or as more diffuse, pervasive circulation (Fig. 9). Channelized flow is related to hydrothermal circulation that travels along fractures, faults, or other high permeability pathways. At the Atlantis Massif, steeply dipping normal faults localize hydrothermal outflow into a series of active vents that lie along a 300 m long east–west lineament and constitute the Lost City hydrothermal field

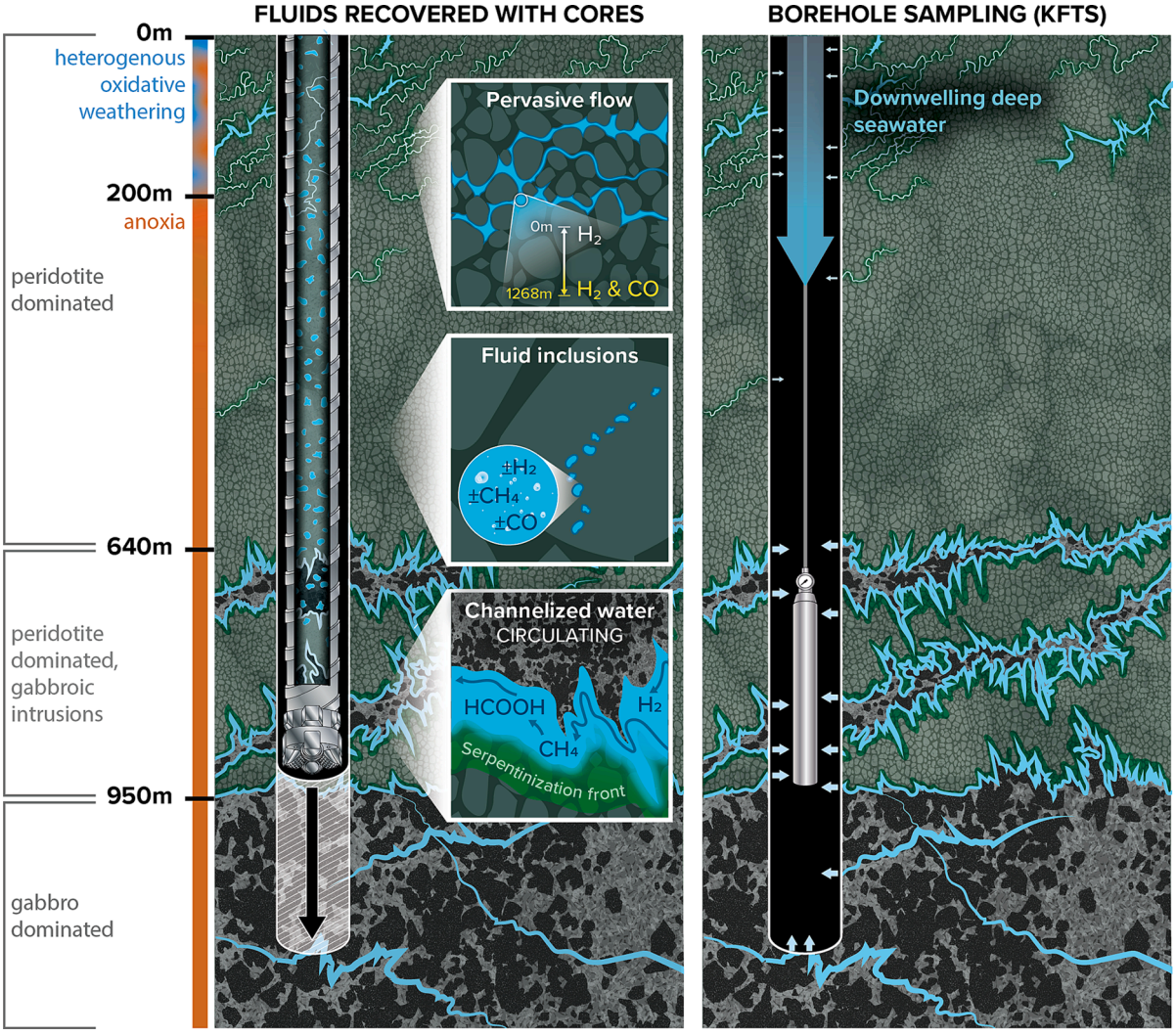

Fig. 9. Schematic of sampling approaches and fluid types from U1601C. While drilling, small volumes of water were recovered with the cores and analyzed for H_2 and CO only (left panel). After drilling, a KFTS sampler was deployed multiple times in the open borehole (right panel). Pervasive flow occurs at scales from around grain boundaries to networks of microfractures at scales of 10 s to 100 s of μm. Channelized flow occurs along fractures, faults, or other high permeability pathways. Mafic intrusions into the host peridotite facilitates fluid flow along the lithological contact. Both pervasive and channelized waters can mobilize volatiles that trapped in fluid inclusions.

(Kelley et al., 2005; Karson et al., 2006). Mathematical models which are consistent with the vent temperatures of Lost City and the heat flow in Hole U1309D suggest depths of circulation ranging from 2.7 kmbsf (Lowell, 2017) to 7 kmbsf (Titarenko and McCaig, 2016).

In addition to fractures and faults, channelized fluid circulation is facilitated where mafic intrusions cut the host peridotite. At the Atlantis Massif, magmatic veins are often heavily hydrothermally altered, and serpentinization is more pervasive in peridotite adjacent to gabbroic contacts (Boschi et al., 2006; Lissenberg et al., 2024; Lang et al., 2025). Macroscopic reaction porosity with wholesale dissolution of pyroxene and plagioclase has been documented at site U1601 (Lang et al., 2025) and may contribute to the storage of formation waters and permeable pathways in the margins of gabbroic intrusions. Serpentine veins commonly follow these pre-existing lithologic contacts and are later overprinted by carbonates, marking sustained fluid flow (Boschi et al., 2008; Ternieten et al., 2021; Lissenberg et al., 2024; Lang et al., 2025). Similar fluid migration along contacts between host peridotite and mafic intrusions are documented at the Galicia margin (ODP Hole 637A; Evans and Baltuck, 1988), the Kane transform fault (ODP Holes 920B and 920D; Andreani et al., 2007; Colat et al., 2023), the Tyrrhenian Sea (IODP Holes U1614C and U1616E; Sanfilippo et al., 2025), and in ophiolites preserved in the geologic record (e.g. Platta nappe in the Swiss Alps; Colat et al., 2019; 2025). Lithological boundaries thus likely represent a common conduit for fluid flow in peridotite-hosted systems.

Superimposed on this focused flow is a second type of circulation that is finer-scale and pervasive. Serpentinized peridotites are characterized by a mesh texture that predates complex veining (Dilek et al., 1997; Beard and Hopkinson, 2000; Andreani et al., 2007; Rouméjon and Cannat, 2014). The mesh texture, which is ubiquitous in Atlantis Massif peridotites (Boschi et al., 2006; Delacour et al., 2008; Rouméjon et al., 2018; Lissenberg et al., 2024; Lang et al., 2025), forms from a network of microfractures at scales of 10 s to 100 s of μm, with some but not all acting as fluid pathways (Rouméjon and Cannat, 2014). Carbonate precipitates along these grain-boundaries have radiocarbon ages spanning > 50 kyr to present, testifying to long-lived pervasive flow (Ternieten et al., 2021).

Both focused and pervasive fluids may receive additional volatiles from primary and secondary fluid inclusions that trap CO_2, CH_4, H_2O, CO, and H_2 (Kelley and Früh-Green, 2001; McDermott et al., 2015; Klein et al., 2019; Andreani et al., 2023). At the Atlantis Massif, fluid inclusions from the gabbroic Holes U1309B and U1309D contain H_2, N_2, CH_3SH, and CH_4 with isotopic compositions (^{13}C, ^{2}H) similar to Lost City fluids (Klein et al., 2019; Andreani et al., 2023). Fluid inclusions were observed in the Hole U1601C rock cores, but their volatile contents are not yet known (Lang et al., 2025). Gases trapped in these inclusions, CH_4 in particular, may have formed during earlier, hotter geologic stages, when temperatures were sufficient to overcome the kinetic barrier that inhibits its synthesis (McDermott et al., 2015; Klein et al., 2019).

These types of fluid flow and volatile storage are dynamically linked. Volatiles released from fluid inclusions can be remobilized into the pervasive flow that permeates a mesh network or into the channelized fluids that flow along fractures (Kelley and Früh-Green, 2001; McDermott et al., 2015; Klein et al., 2019). Fluids channeled through fractures can diffuse laterally away from the flow channel into the pervasive regime of the rock matrix leading to mineral alteration, and conversely diffusion or slow advection of mobile components such as H_2 back into the flow channels (Ague, 2014). Over time, an initial pervasive phase of serpentinization can transition to focused flow along localized pathways to form 100 m to 1 km sized cells (Rouméjon et al., 2018).

Our sampling appears to have captured both channelized and pervasive fluids. The deepest fluids from the open borehole carry micromolar ∑formate together with millimolar H_2 and CH_4, and their isotopic signatures match the channelized fluids venting from the carbonate-brucite chimneys at Lost City (Table 1). Within 60 h, formation fluids had largely displaced the freshwater initially pumped into the borehole (Section 4.4.1), indicating rapid fluid flow. This exchange occurred in the borehole's deepest section, suggesting that channelized flow is more significant at greater depths. The greater abundance of gabbroic intrusions at depth (Lang et al., 2025; Lissenberg et al., 2024) may enhance channelized flow by providing lithologic boundaries that act as preferential fluid pathways.

Pervasive fluids are also present throughout the system. In the shallowest intervals of the open borehole, micromolar concentrations of H_2 and ∑formate are detected, while CH_4 and CO are notably absent. Since these shallow volatiles cannot be attributed to the upwelling of deep fluids (see Section 4.4.2), they are likely generated through local interaction with the surrounding rock. High-resolution sampling of the core catcher fluids likely captured predominantly pervasive fluids, as the channelized fluids are confined to deeper sections of the borehole. These pervasive fluids likely persist at depth alongside or between zones of channelized flow. The core catcher fluids exhibit volatile compositions distinct from the open borehole fluids, with higher CO concentrations but significantly lower H_2 concentrations. These differences suggest a separate fluid source that has equilibrated under local conditions, likely representing the pervasive flow.

6. Conclusion and implications

Two distinct hydrologic regimes emerged from our downhole profiles of H_2, CH_4, ∑CO_2, CO, ∑formate, Rn, and $^{87}Sr/^{86}Sr$. The deep borehole is supplied by fluids with 100 s of micromolar H_2 and CH_4 plus 10 s of micromolar ∑formate that closely mirror the chemistry and isotopic signatures of LCHF vent fluids. Although the borehole does not penetrate the full 3–7 km depth predicted for the deepest portion of LCHF circulation (Lowell, 2017; Titarenko and McCaig, 2016), the isotopic overlap suggests the deepest fluids are controlled by similar water–rock reactions or may even be a portion of the circulation cell. Mafic intrusions enhance permeability and facilitate conduits for these focused hydrothermal fluids.

Superimposed on this focused flow is a pervasive network that also sustains circulation through the surrounding rock matrix. Micromolar H_2 and ∑formate persist even at the shallowest depths where temperatures are too low for rapid serpentinization, implying low temperature in situ water rock reactions and/or contributions from fluid inclusions sustain their widespread availability. Deeper in the borehole, these pervasive fluids host CO, where conditions favor its formation such as higher temperatures and, potentially, lower pHs due to the larger influence of gabbroic intrusions.

The availability of H_2 and distributions of C1 compounds impacts the potential for the ultramafic subseafloor to host life. Our results predict that H_2-based chemoautotrophy and metabolism of C1 compounds could be active throughout the Atlantis Massif, if the combination of extreme pH and temperature is not limiting (Lang & Brazelton, 2020). While ∑CO_2 is low in the deepest borehole samples, our results indicate that ∑formate and CO are available as dissolved carbon feedstocks. The reduction of either species with H_2 would provide thermodynamic energy for biological synthesis reactions. Although chemoautotrophs likely to be active in the subsurface were not detected in shallow cores recovered during Expedition 357 (Goordial et al., 2021; Motamedi et al., 2020; Quéméneur et al., 2019), the deeper samples reported here may contain microbial communities that more closely resemble those of LCHF hydrothermal fluids, which are dominated by putative methanogens and sulfate-reducing bacteria (Brazelton et al., 2022). Furthermore, chemoautotrophs including acetogens and methanogens have been identified in the rocky subsurface of continental ultramafic systems (Colman et al., 2022; Fones et al., 2021; Suzuki et al., 2024) and LCHF chimneys and fluids (Brazelton et al., 2022), but are rarer in shallow cores recovered from the Atlantis Massif during the previous Expedition 357, where genes and organisms associated with heterotrophy dominate (Goordial et al., 2021; Motamedi et al., 2020; Quéméneur et al., 2019). Since H_2 is distributed across a wide range of lithologies, niches will develop that are buffered by the local mineralogy, resulting in differing

pH and availability of important chemical species such as $\sum CO_2$. Future studies will test whether these conditions result in an energy-rich environment with heterogenous chemical and thermal conditions for life to exploit.

Finally, geologically produced H_2 is an emerging target for energy resource exploitation (e.g., IEA, 2021, Hand, 2023; Templeton et al., 2024). Our results indicate that in addition to mM H_2 concentrations in channeled hydrothermal fluids, H_2 could be pervasively distributed at lower concentrations throughout the Atlantis Massif.

Data availability

Data for all tables and figures has been uploaded to Mendeley Data and can be found at https://doi.org/10.17632/kc8npzbw4n.1.

CRediT authorship contribution statement

Susan Q. Lang: Writing – review & editing, Writing – original draft, Visualization, Validation, Supervision, Resources, Project administration, Methodology, Investigation, Funding acquisition, Formal analysis, Data curation, Conceptualization. **C. Geoffrey Wheat:** Writing – review & editing, Writing – original draft, Visualization, Validation, Resources, Methodology, Investigation, Funding acquisition, Formal analysis, Data curation, Conceptualization. **Kristin L. Dickerson:** Writing – review & editing, Writing – original draft, Visualization, Validation, Formal analysis, Data curation. **Mark K. Reagan:** Writing – review & editing, Writing – original draft, Resources, Formal analysis, Data curation. **Ivan P. Savov:** Writing – review & editing, Writing – original draft, Visualization, Resources, Funding acquisition, Formal analysis, Data curation, Conceptualization. **Jordyn A. Robare:** Writing – review & editing, Investigation, Formal analysis, Data curation. **William J. Brazelton:** Writing – review & editing, Investigation, Formal analysis, Data curation. **Johanna Suhonen:** Writing – review & editing, Validation, Formal analysis, Data curation. **Oscar Cavazos:** Writing – review & editing, Investigation, Formal analysis, Data curation. **Andrew McCaig:** Writing – review & editing, Project administration, Investigation, Funding acquisition, Formal analysis, Data curation, Conceptualization. **Peter Blum:** Writing – review & editing, Project administration, Methodology, Investigation, Formal analysis, Data curation. **Natsue Abe:** Writing – review & editing, Investigation, Funding acquisition, Formal analysis, Data curation, Conceptualization. **Rémi Coltat:** Writing – review & editing, Investigation, Formal analysis, Data curation. **Jeremy R. Deans:** Writing – review & editing, Investigation, Formal analysis, Data curation. **Marguerite Godard:** Writing – review & editing, Investigation, Funding acquisition, Formal analysis, Data curation. **Barbara E. John:** Writing – review & editing, Investigation, Funding acquisition, Formal analysis, Data curation. **Frieder Klein:** Writing – review & editing, Investigation, Formal analysis, Data curation. **Rebecca Kuehn:** Writing – review & editing, Investigation, Formal analysis, Data curation. **Kuan-Yu Lin:** Writing – review & editing, Investigation, Formal analysis, Data curation. **C. Johan Lissenberg:** Writing – review & editing, Investigation, Funding acquisition, Formal analysis, Data curation. **Haiyang Liu:** Writing – review & editing, Investigation, Formal analysis, Data curation. **Ethan L. Lopes:** Writing – review & editing, Investigation, Formal analysis, Data curation. **Toshio Nozaka:** Writing – review & editing, Investigation, Formal analysis, Data curation. **William Osborne:** Writing – review & editing, Investigation, Formal analysis, Data curation. **Andrew J. Parsons:** Writing – review & editing, Investigation, Formal analysis, Data curation. **Vamdev Pathak:** Writing – review & editing, Investigation, Formal analysis, Data curation. **Jessica Rodgers:** Writing – review & editing, Investigation, Formal analysis, Data curation. **Jeffrey S. Seewald:** Writing – review & editing, Methodology, Formal analysis, Data curation. **Kenneth W. Sims:** Writing – review & editing, Methodology. **Gordon Southam:** Writing – review & editing, Investigation, Formal analysis, Data curation. **Sean Sylva:** Writing – review & editing, Investigation, Formal analysis, Data curation. **Fengping Wang:** Writing – review & editing, Investigation, Formal analysis, Data curation.

Declaration of competing interest

The authors declare that they have no known competing financial interests or personal relationships that could have appeared to influence the work reported in this paper.

Dr. Freider Klein is an Associate Editor for Geochimica et Cosmochimica Acta and was not involved in the editorial review or the decision to publish this article.

Acknowledgements

We thank the dedicated captain, crew, and technical staff of the JOIDES Resolution and Charin Park (WHOI) for illustrating Fig. 9. Funding: This research used samples and data provided by the International Ocean Discovery Program (IODP). Funding for the operation and management of the scientific drilling vessel JOIDES Resolution was provided by the US National Science Foundation (NSF) (award OCE, 1326927). Funding to join Expedition 399 was provided by NSF (grant OCE, 1450528) for the US Science Support Program Office associated with the International Ocean Discovery Program [USSSP-IODP subcontract 22O(GG009393-04) to S.Q.L., M.K.R., J.R.D., F.K., B.E.J., E.L. L., W.J.B., K.L.D., C.G.W., J.A.R., and K.-Y.L.], UK Natural Environment Research Council (grants NE/X019098/1 to C.J.L., NE/Y001737/1 to A. M.M., NE/Y002350/1 to A.J.P., and NE/Z000424/1 to I.P.S.); Juan de la Cierva fellowship (FJC2021-047190-I to R.C.) funded by the Spanish Ministerio de Ciencia e Innovación and the Agencia Estatal de Investigación (MCIN/AEI/10.13039/ 501100011033); IODP France (to R.C., M.G.); ANR Institut National des Sciences de l'Univers-CNRS (grant ANR-22-EXOR-0001 Origins to M.G.); National Natural Science Foundation of China (grant 42373003 to H.L.); Japan Society for the Promotion of Science (grant KAKENHI 23K03528 and 20H02005 to T.N.), Australia New Zealand International Consortium (ANZIC) IODP (to G. S.); IODP-China Office and Natural Science Foundation of China (grant 92251303 to F.W.); IODP Germany (to R.K.), J-DESC (Japan Drilling Earth Science Consortium to N.A.), and National Centre for Polar and Ocean Research, Ministry of Earth Sciences, Government of India (to V. P.). Shore based analytical work was supported by USSSP-IODP subcontract 22O (GG009393-04) to S.Q.L. and UK Natural Environment Research Council NE/Y002415/1 to I.P.S. We acknowledge Associate Editor Benjamin Tutolo and three anonymous reviewers whose comments improved an earlier version of the manuscript.

Appendix A. Supplementary material

Supplemental material includes a discussion on the potential role of fluid inclusions as the source of detected hydrogen and two figures with additional borehole temperature profiles.

Supplementary material to this article can be found online at https://doi.org/10.1016/j.gca.2025.09.024.

References

Abrajano, T.A., Sturchio, N.C., Bohlke, J.K., Lyon, G.L., Poreda, R.J. and Stevens, C.M., 1988. Methane-hydrogen gas seeps, Zambales Ophiolite, Philippines: Deep or shallow origin? In: M. Schoell (Guest-Editor), Origins of Methane in the Earth. Chem. Geol., 71: 211-222.

Ague, J.J. (2014) Fluid flow in the deep crust. Treatise on Geochemistry (2nd Edition) Eds. Holland, H.D., Turekian, K.K.

Albert, D.B., Martens, C.S., 1997. Determination of low-molecular-weight organic acid concentrations in seawater and pore-water samples via HPLC. Mar. Chem. 56 (1–2), 27–37.

Allen, D.E., Seyfried Jr., W.E., 2003. Compositional controls on vent fluids from ultramafic-hosted hydrothermal systems at midocean ridges: an experimental study at 400°C, 500 bars. Geochim. Cosmochim. Acta 67 (8), 1531–1542.

Allis, R., Gwynn, M., Hardwick, C., & Moore, J. (2018). The Challenge of Correcting Bottom-Hole Temperatures—An Example from FORGE 58-32, near Mifford Utah. in: Proceedings, 43rd workshop on geothermal reservoir engineering. SGO-TR-213.

Altwegg, K., Balsiger, H., Berthelier, J.J., Bieler, A., Calmonte, U., Fuselier, S.A., Goesmann, F., Gasc, S., Gombosi, T.I., Le Roy, L., de Keyser, J., 2017. Organics in comet 67P-a first comparative analysis of mass spectra from ROSINA-DFMS, COSAC and Ptolemy. MNRAS 469. S130 S141.

Andreani, M., Mevel, C., Boullier, A.-M., Escartin, J., 2007. Dynamic control on serpentine crystallization in veins: constraints on hydration processes in oceanic peridotite. Geochem. Geophys. Geosyst. 8 (2), 1–24.

Andreani, M., Montagnac, G., Fellah, C., Hao, J., Vandier, F., Daniel, I., Pisapia, C., Galipaud, J., Lilley, M.D., Früh-Green, G.L., Borensztajn, S., Menez, B., 2023. The rocky road to organics needs drying. Nat. Commun. 14 (347), 1–12.

Aquino, K.A., Früh-Green, G.L., Rickli, J., Bernasconi, S.M., Lang, S.Q., Lilley, M.D., Butterfield, D.A., 2022. Multi-stage evolution of the lost City hydrothermal vent fluids. Geochim. Cosmochim. Acta 332, 239–262.

Barnes, I., LaMarche, V.C., Himmelberg, G., 1967. Geochemical Evidence of Present-Day Serpentinization. Science 156 (3776), 830–832.

Beard, J.S., Hopkinson, L., 2000. A fossil, serpentinization-related hydrothermal vent, ocean drilling program leg 173, site 1068 (Iberia Abyssal Plain): some aspects of mineral and fluid chemistry. J. Geophys. Res. 105 (B7), 16527–16539.

Biver, N., Bockelée-Morvan, D., 2019. Complex organic molecules in comets from remote-sensing observations at millimeter wavelengths. ACS Earth Space Chem. 3 (8), 1550–1555.

Blackman, D., Collins, J., 2010. Lower crustal variability and the crust/mantle transition at the Atlantis Massif oceanic core complex. Geophys. Res. Lett. 37. Article L24303.

Blackman, D.K., Cann, J.R., Janssen, B., Smith, D.K., 1998. Origin of extensional core complexes: evidence from the Mid-Atlantic Ridge at Atlantis Fracture Zone. J. Geophys. Res. -Solid Earth 103 (B9), 21315–21333.

Blackman, D.K., Karson, J.A., Kelley, D.S., Cann, J.R., Früh-Green, G.L., Gee, J.S., Hurst, S.D., John, B.E., Morgan, J., Nooner, S.L., Ross, D.K., 2002. Geology of the Atlantis Massif (Mid-Atlantic Ridge, 30 degrees N): Implications for the evolution of an ultramafic oceanic core complex. Mar. Geophys. Res. 23 (5–6), 443–469.

Blackman, D.K., Ildefonse, B., John, B.E., Ohara, Y., Miller, D.J., MacLeod, C.J., and the Expedition 304/305 Scientists, 2006. Proceedings of the Integrated Ocean Drilling Program, 304/305: College Station, TX (Integrated Ocean Drilling Program Management International, Inc.). doi: 10.2204/iodp.proc.304305.2006.

Blackman, D.K., Ildefonse, B., John, B.E., Ohara, Y., Miller, D.J., Abe, N., Abratis, M.W., Andal, E.S., Andreani, M., Awaji, S., Beard, J.S., Brunelli, D., Charney, A., Christie, D., Delacour, A.G., Delius, H., Drouin, M., Einaudi, F., Escartin, J., Frost, B. R., Fryer, P.B., Gee, J.S., Godard, M., Grimes, C.B., Halfpenny, A., Hansen, H.-E., Harris, A.C., Tamura, A., Hayman, N.W., Hellebrand, E., Hirose, T., Hirth, J.G., Ishimaru, S., Johnson, K.T.M., Karner, G.D., Linek, M., Maeda, J., Mason, O.U., MacLeod, C.J., McCaig, A.M., Michibayashi, K., Morris, A., Nakagawa, T., Nozaka, T., Rosner, M., Searle, R.C., Suhr, G., Tominaga, M., von der Handt, A., Yamasaki, T., Zhao, X., 2011. Drilling constraints on lithospheric accretion and evolution at Atlantis Massif, Mid-Atlantic Ridge 30°N. J. Geophys. Res. 116 (B07103).

Blackman, D., Slagle, A., Guerin, G., Harding, A., 2014. Geophysical signatures of past and present hydration within a young oceanic core complex. Geophys. Res. Lett. 41, 1179–1186.

Board, S.S., 2019. National Academies of Sciences, Engineering, and Medicine. An Astrobiology Strategy for the Search of Life in the Universe. National Academies Press.

Boschi, C., Früh-Green, G.L., Delacour, A., Karson, J.A., Kelley, D.S., 2006. Mass transfer and fluid flow during detachment faulting and development of an oceanic core complex, Atlantis Massif (MAR 30 degrees N). Geochem. Geophys. Geosyst. 7, 39. Article Q01004. https://doi-org.pallas2.tcl.sc.edu/10.1029/2005gc001074.

Bradley, A.S., Summons, R.E., 2010. Multiple origins of methane at the lost city hydrothermal field. Earth Planet. Sci. Lett. 297 (1–2), 34–41.

Brazelton, W.J., Thornton, C.N., Hyer, A., Twing, K.I., Longino, A.A., Lang, S.Q., Lilley, M.D., Früh-Green, G.L., Schrenk, M.O., 2017. Metagenomic identification of active methanogens and methanotrophs in serpentinite springs of the Voltri Massif, Italy. Peerj 5 e2945.

Brazelton, W.J., McGonigle, J.M., Motamedi, S., Pendleton, H.L., Twing, K.I., Miller, B. C., Lowe, W.J., Hoffman, A.M., Prator, C.A., Chadwick, G.L., Anderson, R.E., 2022. Metabolic strategies shared by basement residents of the lost city hydrothermal field. Appl. Environ. Microbiol. 88 (17), e0092922.

Bullard, E.C., 1947. The time necessary for a bore hole to attain temperature equilibrium. Geophys. J. Int. 5, 127–130.

Cann, J.R., Blackman, D.K., Smith, D.K., McAllister, E., Janssen, B., Mello, S., Avgerinos, E., Pascoe, A.R., Escartin, J., 1997. Corrugated slip surfaces formed at ridge-transform intersections on the Mid-Atlantic Ridge. Nature 385 (6614), 329–332.

Charlou, J.L., Donval, J.P., Fouquet, Y., Jean-Baptiste, P., Holm, N., 2002. Geochemistry of high H_2 and CH_4 vent fluids issuing from ultramafic rocks at the Rainbow hydrothermal field (36°14′N, MAR). Chem. Geol. 191, 345–359.

Charlou, J. L., Donval, J. P., Konn, C., Ondreas, H., Fouquet, y., Jean-Baptiste, P., & Fourre, E. (2010). High Production and Fluxes of H2 and CH4 and Evidence of Abiotic Hydrocarbon Synthesis by Serpentinization in Ultramafic-Hosted Hydrothermal Systems on the Mid-Atlantic Ridge. In Diversity of Hydrothermal Systems on Slow Spreading Ocean Ridges (Vol. 188). Geophys. Monogr. Ser.

Colman, D.R., Kraus, E.A., Thieringer, P.H., Rempfert, K., Templeton, A.S., Spear, J.R., Boyd, E.S., 2022. Deep-branching acetogens in serpentinized subsurface fluids of Oman Proc. Nat. Acad. Sci. 119 (42), e2206845119.

Colman, D.R., Templeton, A.S., Spear, J.R., Boyd, E.S., 2025. Microbial ecology of serpentinite-hosted ecosystems. ISME J. 19 (1).

Coltat, R., Branquet, Y., Gautier, P., Campos Rodriguez, H., Poujol, M., Pelleter, E., McClenaghan, S., Manatschal, G., Boulvais, P., 2019. Unravelling the root zone of ultramafic-hosted black smokers-like hydrothermalism from an Alpine analog. Terra Nova 31, 549–561.

Coltat, R., Andreani, M., Patten, C.G.C., Godard, M., Debret, B., Escartin, J., 2023. Origin of Fe-Ca-metasomatism in exhumed Mantle Rocks at the MARK area (23°N, ODP Leg 153) and implications on the formation of ultramafic-hosted seafloor massive sulfide deposits. Geochem. Geophys. Geosyst. 24, e2023GC010894.

Coltat, R., Patten, C.G.C., Padrón-Navarta, J.A., Hochscheid, F., Ulrich, M., Branquet, Y., Boulvais, P., Garrido, C.J., 2025. Constraints on Fe-Ca metasomatism in mineralized mantle rocks: Insights from in-situ geochemistry and thermodynamic modeling. Chem. Geol. 687, 122826.

Delacour, A., Früh-Green, G.L., Frank, M., Gutjahr, M., Kelley, D.S., 2008. Sr- and Nd-isotope geochemistry of the Atlantis Massif (30N, MAR): implications for fluid fluxes and lithospheric heterogeneity. Chem. Geol. 254, 19–35.

de Ronde, C.E.J., Humphris, S.E., Höfig, T.W., Brandl, P.A., Cai, L., Cai, Y., Caratori Tontini, F., Deans, J.R., Farough, A., Jamieson, J.W., Kolandaivelu, K.P., Kutovaya, A., Labonté, J.M., Martin, A.J., Massiot, C., McDermott, J.M., McIntosh, I.M., Nozaki, T., Pellizari, V.H., Reyes, A.G., Roberts, S., Rouxel, O., Schlicht, L.E.M., Seo, J.H., Straub, S.M., Strehlow, K., Takai, K., Tanner, D., Tepley III, F.J., and Zhang, C., 2019. Expedition 376 methods. In de Ronde, C.E.J., Humphris, S.E., Höfig, T.W., and the Expedition 376 Scientists, Brothers Arc Flux. Proceedings of the International Ocean Discovery Program, 376: College Station, TX (International Ocean Discovery Program). https://doi.org/10.14379/iodp.proc.376.102.2019.

Dickson, A.G., 1990. Thermodynamics of the dissociation of boric acid in synthetic seawater from 273.15 to 318.15 K. Deep-Sea Res. 37 (5), 755–766.

Dilek, Y., Goulton, A., Hurst, S.D. (1997) Serpentinization and hydrothermal veining in peridotites at Site 920 in the Mark area. In: Proceedings of the Ocean Drilling Program, Scientific Results (Eds. Karson, J.A., Cannat, M., Miller, D.J., and Elthon, D.). 153: 35 - 59.

Dowdle, W.L., Cobb, W.M., 1975. Static formation temperature from well logs – empirical method. J. Petrol. Tech. 27, 1326–1330.

Druffel, E.R.M., Griffin, S., Coppola, A.I., Walker, B.D., 2016. Radiocarbon in dissolved organic carbon of the Atlantic Ocean. Geopys. Res. Lett. 43, 5279–5286.

Drury, M.J., 1984. On a possible source of error in extracting equilibrium formation temperatures from borehole BHT data. Geothermics 13 (3), 175–180.

Ehrenfreund, P., Charnley, S., 2000. Organic molecules in the interstellar medium, comets, and meteorites: a voyage from dark clouds to the early earth. Ann. Review Astronomy Astrophys. 38, 427.

Eickenbusch, P., Takai, K., Sissman, O., Suzuki, S., Menzies, C., Sakai, S., Sansjofre, P., Tasumi, E., Bernasconi, S.M., Glombitza, C., Jorgensen, B.B., Morono, Y., Lever, M. A., 2019. Origin of short-chain organic acids in serpentinite mud volcanoes of the mariana convergent margin. Front. Microbiol. 10, 1729.

Escartín, J., John, B., Cannat, M., Olive, J., Cheadle, M., Früh-Green, G., Cotterill, C., 2022. Tectonic termination of oceanic detachment faults, with constraints on tectonic uplift and mass wasting related erosion rates. Earth Planet. Sci. Lett. 584, 117449.

Espinosa-Paredes, G., Garcia-Gutierrez, A., 2003. Estimation of static formation temperatures in geothermal wells. Energ. Conver. Manage. 44 (8), 1343–1355.

Etiope, G., Whiticar, M.J., 2019. Abiotic methane in continental ultramafic rock systems: towards a genetic model. Appl. Geochem. 102, 139–152.

Etiope, G., Schoell, M., Hosgormez, H., 2011. Abiotic methane flux from the Chimaera seep and Tekirova ophiolites (Turkey): Understanding gas exhalation from low temperature serpentinization and implications for Mars. Earth Planet. Sci. Lett. 310, 96–104.

Evans, C.A. and Baltuck, M. (1988) Low temperature alteration of peridotite, Hole 637A. In G. Boillot and E.L. Winterer (Eds.), Proceedings of the Ocean Drilling Program, Scientific Results. 103: 235-239.

Fones, E., Colman, D., Kraus, E., Stepanauskas, R., Templeton, A., Spear, J., Boyd, E., 2021. Diversification of methanogens into hyperalkaline serpentinizing environments through adaptations to minimize oxidant limitation. ISME J. 15, 1121–1135.

Früh-Green, G.L., Orcutt, B.N., Green, S.L., Cotterill, C., Morgan, S., Akizawa, N., Bayrakci, G., Behrmann, J.-H., Boschi, C., Brazelton, W.J., Cannat, M., Dunkel, K.G., Escartin, J., Harris, M., Herrero-Bervera, E., Hesse, k., John, B.E., Lang, S.Q., Lilley, M.D., Liu, H.-Q., Mayhew, L.E., McCaig, A.M., Menez, B., Morono, Y., Quéméneur, M., Rouméjon, S., Sandaruwan Ratnayake, A., 1205 Schrenk, M.O., Schwarzenbach, E.M., Twing, K.I., Weis, D., Whattham, S.A., Williams, M., Zaho, R., 2017. Expedition 357 Summary. In Früh-Green, G.L., Orcutt, B.N., Green, S.L., Coterill, C., and the Expedition 357 Scientists, Atlantis Massif Serpentinization and Life. Proceedings of the International Ocean Discovery Program, 357. College Station, TX. https://doi.org/10.14379/iodp.proc.357.101.2017.

Früh-Green, G.L., Orcutt, B.N., Rourméjon, S., Lilley, M.D., Morono, Y., Cotterill, C., Green, S., Escartin, J., John, B.E., McCaig, A.M., Cannat, M., Ménez, B., Schawarzenbach, E.M., Williams, M.J., Morgan, S., Lang, S.Q., Schrenk, M.O., Brazelton, W.J., Akizawa, N., Boschi, C., Dunkel, K.G., Quéméneur, M., Whattman, S. A., Mayhew, L., Harris, M., Bayrakci, G., Behrmann, J.-H., Herrero-Bervera, E., Hesse, K., Liu, H.-Q., Ratnayake, A.S., Twing, K., Weis, D., Zhao, R., Bilenker, L., 2018. Magmatism, serpentinization and life: Insights through drilling the Atlantis Massif (IODP Expedition 357). Lithos 323, 137–155.

Früh-Green, G.L., Kelley, D.S., Lilley, M.D., Cannat, M., Chavagnac, V., Baross, J.A., 2022. Diversity of magmatism, hydrothermal processes and microbial interactions at mid-ocean ridges. Nat. Rev. Earth Environ. 3 (12), 852–871.

German, C., Lang, S.Q., Fitzsimmons, Jessica, 2024. Hydrothermal Processes. In: Anbar, A.D., Weis, D. (Eds.), Treatise on Geochemistry, (3rd ed.). Elsevier.
Gieskes, J.M., Gamo, T., Brumsack, H., 1991. Chemical methods for interstitial water analysis aboard JOIDES Resolution. ODP Tech. Note 15.
Glavin, D.P., Dworkin, J.P., Alexander, C.M.O., Aponte, J.C., Baczynski, A.A., Barnees, J. J., et al., 2025. Abundant ammonia and nitrogen-rich soluble organic matter in samples from asteroid (101955) Bennu. Nat. Astron 9, 199–210.
Glein, C.R., Baross, J.A., Waite, J.H., 2015. The pH of Enceladus' ocean. Geochim. Cosmochim. Acta 162, 202–219.
Goesmann, F., Rosenbauer, H., Bredehöft, J.H., Cabane, M., Ehrenfreund, P., Gautier, T., Giri, C., Krüger, H., Le Roy, L., MacDermott, A.J., McKenna-Lawlor, S., 2015. Organic compounds on comet 67P/Churyumov-Gerasimenko revealed by COSAC mass spectrometry. Science 349 (6247). Article aab0689.
Goordial, J., D'angelo, T., Labonté, J.M., Poulton, N.J., Brown, J.M., Stepanauskas, R., Früh-Green, G.L., Orcutt, B.N., 2021. Microbial diversity and function in shallow subsurface sediment and oceanic lithosphere of the Atlantis Massif. MBio 12. Article e00490–21.
Grimes, C., John, B., Cheadle, M., Wooden, J., 2008. Protracted construction of gabbroic crust at a slow spreading ridge: Constraints from ^{206}Pb-^{238}U zircon ages from Atlantis Massif and IODP Hole U1309D (30°N, MAR). Geochem. Geophys. Geosyst. 9. Article Q08012.
Grozeva, N.G., Klein, F., Seewald, J.S., Sylva, S.P., 2020. Chemical and isotopic analyses of hydrocarbon-bearing fluid inclusions in olivine-rich rocks. Phil. Trans. R. Soc. A 378, 20180431. https://doi.org/10.1098/rsta.2018.0431.
Hand, E., 2023. Hidden hydrogen: does Earth hold vast stores of a renewable, carbon-free fuel? Science 379, 6633.
Harding, A.J., Arnulf, A.F., Blackman, D.K., 2016. Velocity structure near IODP Hole U1309D, Atlantis Massif, from waveform inversion of streamer data and borehole measurements. Geochem. Geophys. Geosyst. 17 (6), 1990–2014.
Heberling, C., Lowell, R.P., Liu, L., Fisk, M.R., 2010. Extent of the microbial biosphere in the oceanic crust. Geochem. Geophys. Geosyst. 11 (8), 1–15.
He, D., Wang, X., Yang, Y., He, R., Zhong, H., Wang, Y., Han, B., Jin, F., 2021. Hydrothermal synthesis of long-chain hydrocarbons up to C_{24} with $NaHCO_3$ assisted stabilizing cobalt. Proc. Nat. Acad. Sci. 118. Article e2115059118.
Hirose, T., Kawagucci, S., Suzuki, K., 2011. Mechanoradical H2 generation during simulated faulting: implications for an earthquake-driven subsurface biosphere. Geophys. Res. Lett. 38. Article L17303.
Huang, Y., Wang, Y., Alexandre, M., Lee, T., Rose-Petruck, C., Fuller, M., Pizzarello, S., 2005. Molecular and compound-specific isotopic characterization of monocarboxylic acids in carbonaceous meteorites. Geochim. Cosmochim. Acta 69 (4), 1073–1084.
IEA (2021) Global hydrogen review 2021. Retrieved from https://iea.blob.core.windows.net/ assets/5bd46d7b-906a-4429-abda-e9c507a62341/GlobalHydrogenReview2021.pdf.
Irvine, W., 1998. Extraterrestrial organic matter: a review. Origins Life Evol. Biospheres 28 (4–6), 365–383.
Jin, B., Luo, L., Xie, L., 2021. Pathways and kinetics for autocatalytic reduction of CO_2 into formic acid with Fe under hydrothermal conditions. ACS OMEGA 6, 11280–11285.
Johnson, J.W., Oelkers, E.H., Helgeson, H.C., 1992. SUPCRT92: a software package for calculating the standard molal thermodynamic properties of minerals, gases, aqueous species, and reactions from 1 to 5000 bar and 0 to 1000 °C. Comput. Geosci. 18, 899–947.
Kadko, D.C., Rosenberg, N.D., Lupton, J.E., Collier, R.W., Lilley, M.D., 1990. Chemical reaction rates and entrainment within the Endeavour Ridge hydrothermal plume. Earth Planet. Sci. Lett. 99, 315–335.
Karson, J.A., Früh-Green, G.L., Kelley, D.S., Williams, E.A., Yoerger, D.R., Jakuba, M., 2006. Detachment shear zone of the Atlantis Massif core complex, Mid-Atlantic Ridge, 30 degrees N. Geochem. Geophys Geosyst 7.
Keir, R.S., 2010. A note on the fluxes of abiogenic methane and hydrogen from mid-ocean ridges. Geophys. Res. Lett. 37. Article L24609.
Kelley, D.S., Früh-Green, G.L., 2001. Volatile lines of descent in submarine plutonic environments: insights from stable isotope and fluid inclusion analyses. Geochimica Et Cosmochimica Acta 65, 3325–3346.
Kelley, D.S., Karson, J.A., Blackman, D.K., FruÈh-Green, G.L., Butterfield, D.A., Lilley, M. D., Olson, E.J., Schrenk, M.O., Roe, K.K., Lebon, G.T., Rivizzigno, P., 2001. An off-axis hydrothermal vent field near the Mid-Atlantic Ridge at 30 degrees N. Nature 412 (6843), 145–149.
Kelley, D.S., Karson, J.A., Fruh-Green, G.L., Yoerger, D.R., Shank, T.M., Butterfield, D.A., Hayes, J.M., Schrenk, M.O., Olson, E.J., Proskurowski, G., Jakuba, M., 2005. A serpentinite-hosted ecosystem: the lost city hydrothermal field. Science 307 (5714), 1428–1434.
Klein, F., Bach, W., McCollom, T., 2013. Compositional controls on hydrogen generation during serpentinization of ultramafic rocks. Lithos 178, 55–69.
Klein, F., Grozeva, N.G., Seewald, J.S., 2019. Abiotic methane synthesis and serpentinization in olivine-hosted fluid inclusions. Proc. Nat. Acad. Sci. 116 (36), 17666–17672.
Kohl, L., Cumming, E., Cox, A., Rietze, A., Morrissey, L., Lang, S.Q., Richter, A., Suzuki, S., Nealson, K.H., Morrill, P.L., 2016. Exploring the metabolic potential of microbial communities in ultra-basic, reducing springs at the Cedars, CA, USA: experimental evidence of microbial methanogenesis and heterotrophic acetogenesis. J. Geophys. Res. Biogeosci. 121, 1203–1220.
Konn, C., Charlou, J.L., Donval, J.P., Holm, N.G., Dehairs, F., Bouillon, S., 2009. Hydrocarbons and oxidized organic compounds in hydrothermal fluids from rainbow and lost city ultramafic-hosted vents. Chem. Geol. 299–314.
Labidi, J., Young, E.D., Giunta, T., Kohl, I.E., Seewald, J., Tang, H., Lilley, M.D., Früh-Green, G.L., 2020. Methane thermometry in deep-sea hydrothermal systems: evidence for re-ordering of doubly-substituted isotopologues during fluid cooling. Geochim. Comochim. Acta 288, 248–261.
Lang, S.Q., Brazelton, W.J., 2020. Habitability of the marine serpentinite subsurface: a case study of the lost city hydrothermal field. Phil. Trans. R. Soc. A 378 (2165). Article 20180429.
Lang, S.Q., Butterfield, D.A., Schulte, M., Kelley, D.S., Lilley, M.D., 2010. Elevated concentrations of formate, acetate and dissolved organic carbon found at the lost City hydrothermal field. Geochim. Cosmochim. Acta 74 (3), 941–952.
Lang, S.Q., Früh-Green, G.L., Bernasconi, S.M., Lilley, M.D., Proskurowski, G., Mehay, S., Butterfield, D.A., 2012. Microbial utilization of abiogenic carbon and hydrogen in a serpentinite-hosted system. Geochim. Cosmochim. Acta 92, 82–99.
Lang, S.Q., Früh-Green, G.L., Bernasconi, S.M., Brazelton, W.J., Schrenk, M.O., McGonigle, J.M., 2018. Deeply-sourced formate fuels sulfate reducers but not methanogens at lost city hydrothermal field. Scientif. Rep. 8. Article 755.
Lang, S.Q., Lilley, M.D., Baumberger, T., Früh-Green, G.L., Walker, S.L., Brazelton, W.J., Kelley, D.S., Elend, M., Butterfield, D.A., Mau, A.J., 2021. Extensive decentralized hydrogen export from the Atlantis Massif. Geology 49 (7), 851–856.
Lang, S.Q., Benitez-Nelson, B., Vincent, M., Soong, R., Kock, F.V., Lysak, D.H., Jenne, A., Simpson, A.J., 2024. Rapid removal and replacement of dissolved organic matter during circulation through ultramafic crust. Earth Planet. Sci. Lett. 629, 118600.
Lang, S.Q., McCaig, A.M., Blum, P., Expedition 399 Scientists (2025) Site U1601. In McCaig, A., Lang, S.Q., Blum, P., and the Expedition 399 Scientists, Building Blocks of Life, Atlantis Massif. Proceedings of the International Ocean Discovery Program, 399. College Station, TX.
Lefeuvre, N., Thomas, E., Truche, L., Donzé, F.V., Cros, T., Dupuy, J., Pinzon-Rincon, L., Rigollet, C., 2024. Characterizing natural hydrogen occurrences in the Paris basin from historical drilling records. Geochem. Geophys. Geosyst. 25. Article e2024GC011501.
Leong, J.A.M., Howells, A.E., Robinson, K.J., Cox, A., Debes, R.V., Fecteau, K., et al., 2021. Theoretical predictions versus environmental observations on serpentinization fluids: lessons from the Samail ophiolite in Oman. J. Geophys. Res.: Solid Earth 126, e2020JB020756.
Leong, J.A., Nielsen, M., McQueen, N., Karolyte, R., Hillegonds, D.J., Ballentine, C., Darrah, T., McGillis, W., Kelemen, P., 2023. H2 and CH4 outgassing rates in the Samail ophiolite, Oman: implications for low-temperature, continental serpentinization rates. Geochim. Cosmochim. Acta. 347, 1–15.
Lin, Y., Heuer, V., Goldhammer, T., Kellermann, M., Zabel, M., Hinrichs, K., 2012. Towards constraining H_2 concentration in subseafloor sediment: a proposal for combined analysis by two distinct approaches. Geochim. Cosmochim. Acta 77, 186–201.
Lissenberg, C.J., McCaig, A.M., Lang, S.Q., Blum, P., Abe, N., Brazelton, W.J., Coltat, R., Deans, J.R., Dickerson, K.L., Godard, M., John, B.E., 2024. A long section of serpentinized depleted mantle peridotite. Science 385, 623–629.
Lowell, R.P., 2017. A fault-driven circulation model for the lost city hydrothermal field. Geophys. Res. Lett. 44 (6), 2703–2709.
Ludwig, K.A., Kelley, D.S., Butterfield, D.A., Nelson, B.K., Früh-Green, G., 2006. Formation and evolution of carbonate chimneys at the lost city hydrothermal field. Geochim. Cosmochim. Acta 70, 3625–3645.
Martin, W., Russell, M.J., 2007. On the origin of biochemistry at an alkaline hydrothermal vent. Phil. Trans. R. Soc. B 362 (1486), 1887–1925.
Mayhew, L.E., Ellison, E.T., McCollom, T.M., Trainor, T.P., Templeton, A.S., 2011. Hydrogen generation from low-temperature water-rock reactions. Nat. Geosci. 6, 478–484.
McCaig, A. M., Lang, S. Q., Blum, P., & Expedition 399 Scientists (2024). Preliminary Report: Building Blocks of Life, Atlantis Massif. In. International Ocean Discovery Program. DOI: doi.org/10.14379/iodp.pr.399.2024.
McCollom, T., Bach, W., 2009. Thermodynamic constraints on hydrogen generation during serpentinization of ultramafic rocks. Geochim. Cosmochim. Acta 73, 856–875.
McCollom, T.M., Seewald, J.S., 2001. A reassessment of the potential for reduction of dissolved CO2 to hydrocarbons during serpentinization of olivine. Geochim. Cosmochim. Acta 65, 3769–3778.
McCollom, T.M., Seewald, J.S., 2003. Experimental constraints on the hydrothermal reactivity of organic acids and acid ions: I. Formic acid and formate. Geochim. Cosmochim. Acta 67 (19), 3625–3644.
McCollom, T.M., Seewald, J.S., 2007. Abiotic synthesis of organic compounds in deep-sea hydrothermal environments. Chem. Rev. 107 (2), 382–401.
McCollom, T.M., Lollar, B.S., Lacrampe-Couloume, G., Seewald, J.S., 2010. The influence of carbon source on abiotic organic synthesis and carbon isotope fractionation under hydrothermal conditions. Geochim. Cosmochim. Acta 74 (9), 2717–2740.
McCollom, T.M., Seewald, J.S., German, C.R., 2015. Investigation of extractable organic compounds in deep-sea hydrothermal vent fluids along the Mid-Atlantic Ridge. Geochim. Cosmochim. Acta 156, 122–144.
McCollom, T.M., Klein, F., Robbins, M., Moskowitz, B., Berquó, T.S., Jöns, N., Bach, W., Templeton, A., 2016. Temperature trends for reaction rates, hydrogen generation, and partitioning of iron during experimental serpentinization of olivine. Geochim. Cosmochim. Acta. 181, 175–200.
McDermott, J.M., Seewald, J.S., German, C.R., Sylva, S.P., 2015. Pathways for abiotic organic synthesis at submarine hydrothermal fields. Proc. Nat. Acad. Sci. 112 (25), 7668–7672.
McDermott, J.M., Sylva, S.P., Ono, S., German, C.R., Seewald, J.S., 2020. Abiotic redox reactions in hydrothermal mixing zones: decreased energy availability for the subsurface biosphere. Proc. Nat. Acad. Sci. 117 (34), 20453–20461.
McGonigle, J.M., Lang, S.Q., Brazelton, W.J., 2020. Genomic evidence for formate metabolism by Chloroflexi as the key to unlocking deep carbon in lost city microbial ecosystems. Appl. Environ. Microbiol. 86 (8), 02583.

Mei, N., Postec, A., Bartoli, M., Vandecasteele, C., Wils, L., Gil, L., Monnin, C., Pelletier, B., Erauso, G. and Quéméneur, M., 2022. Methanobacterium alkalithermotolerans sp. nov., a novel alkaliphilic and hydrogen-utilizing methanogen isolated from an alkaline geothermal spring (La Crouen, New Caledonia). International journal of systematic and evolutionary microbiology, 72(10), p.005554.

Miller, S.L., 1953. A production of amino acids under possible primitive Earth conditions. Science 117 (3046), 528–529.

Miller, H.M., Chaudhry, N., Conrad, M.E., Bill, M., Kopf, S.H., Templeton, A.S., 2018. Carbon isotope variability during methanogenesis under alkaline conditions. Geochim. Cosmochim. Acta 237, 18–31.

Moody, J.B., 1976. Serpentinization: a review. Lithos 9, 125–138.

Moore, W.S., Frankle, J.D., Benitez-Nelson, C.R., Früh-Green, G.L., Lang, S.Q., 2021. Activities of 223Ra and 226Ra in fluids from the lost city hydrothermal field require short fluid residence times. J. Geophys. Res.: Oceans 126 (12) e2021JC017886.

Motamedi, S., Orcutt, B., Früh-Green, G., Twing, K., Pendleton, H., Brazelton, W., 2020. Microbial residents of the Atlantis Massif's Shallow Serpentinite subsurface. Appl. Environ. Microbiol. 86. Article e00356–20.

National Research Council (1990) The Role of Fluids in Crustal Processes. Washington, DC: The National Academies Press. doi: 10.17226/1346.

Neal, C., Stanger, G., 1983. Hydrogen generation form mantle source rocks in Oman. Earth Planet. Sci. Lett. 66, 315–320.

Neubeck, A., Thanh Duc, N., Bastviken, D., Crill, P., Holm, N.G., 2011. Formation of H2 and CH4 by weathering of olivine at temperatures between 30 and 70C. Geochem. Trans. 12, 6. http://www.geochemicaltransactions.com/content/12/1/6.

Okland, I., Huang, S., Thorseth, I.H., Pedersen, 2014. Formation of H2, CH4 and N-species during low-temperature experimental alteration of ultramafic rocks. Chem. Geol. 387, 22–34.

Orcutt, B.N., Sylvan, J.B., Knab, N.J., Edwards, K.J., 2011. Microbial ecology of the Deark Ocean above, at, and below the seafloor. Microbiol. Mol. Biol. Rev. 75 (2), 361.

Osselin, F., Soulaine, C., Fauguerolles, C., Gaucher, E., Scaillet, B., Pichavant, M., 2022. Orange hydrogen is the new green. Nat. Geosci. 15 (10), 765–769.

Palandri, J.L., Reed, M.H., 2004. Geochemical models of metasomatism in ultramafic systems: serpentinization, rodingitization, and sea floor carbonate chimney precipitation. Geochim. Cosmochim. Acta 68 (5), 1115–1133.

Peter, J., Nordheim, T., Hand, K., 2024. Detection of HCN and diverse redox chemistry in the plume of Enceladus. Nat. Astronomy 8 (2), 150.

Pisapia, C., Gérard, E., Gérard, M., Lecourt, L., Lang, S.Q., Pelletier, B., Payri, C., Monnin, C., Guentas, L., Postec, A., Quéméneur, M., Erauso, G., Ménez, B., 2017. Mineralization filamentous bacteria from the Prony Bay Hydrothermal Field give new insights to the functioning of serpentinization-based subseafloor ecosystems. Front. Microbiol. 8, 57.

Proskurowski, G., Lilley, M.D., Kelley, D.S., Olson, E.J., 2006. Low temperature volatile production at the lost City Hydrothermal Field, evidence from a hydrogen stable isotope geothermometer. Chemical Geology 229 (4), 331–343.

Proskurowski, G., Lilley, M.D., Seewald, J.S., Früh-Green, G.L., Olson, E.J., Lupton, J.E., Sylva, S.P., Kelley, D.S., 2008. Abiogenic hydrocarbon production at lost city hydrothermal field. Science 319 (5863), 604–607.

Quéméneur, M., Erauso, G., Frouin, E., Zeghal, E., Vandecasteele, C., Ollivier, B., Tamburini, C., Garel, M., Ménez, B., Postec, A., 2019. Hydrostatic pressure helps to cultivate an original anaerobic bacterium from the Atlantis massif Subseafloor (IODP Expedition 357): *Petrocella atlantisensis* gen. nov. sp. nov. Frontiers in Microbiology 10. Article 1497.

Reeves, E.P., McDermott, J.M., Seewald, J.S., 2014. The origin of methanethiol in midocean ridge hydrothermal fluids. Proc. Nat. Acad. Sci 111 (15), 5474–5479.

Rempfert, K.R., Miller, H.M., Bompard, N., Nothaft, D., Matter, J.M., Kelemen, P., Fierer, N., Templeton, A.S., 2017. Geological and geochemical controls on subsurface microbial life in the Samail ophiolite, Oman. Front. Microbiol. 8, 00056.

Roumejon, S., Cannat, M., 2014. Serpentinization of mantle-derived peridotites at mid-ocean ridges: mesh texture development in the context of tectonic exhumation. Geochem. Geophys. Geosyst. 15, 2354–2379.

Rouméjon, S., Früh-Green, G.L., Orcutt, B.N., and IODP Expedition 357 Science Party (2018) Alteration Heterogeneities in Peridotites Exhumed on the Southern Wall of the Atlantis Massif, (IODP Expedition 357) J. Petrol.. 1-29.

Sanfilippo, A., Pandey, A., Akizawa, N., Poulaki, E., Cunningham, E., Bickert, M., et al., 2025. Heterogeneous Earth's mantle drilled at an embryonic ocean. Nature Communications. 16 (2016), 1–11.

Schrenk, M.O., Kelley, D.S., Bolton, S.A., Baross, J.A., 2004. Low archaeal diversity linked to subseafloor geochemical processes at the Lost City Hydrothermal Field, Mid-Atlantic Ridge. Environ. Microbiol. 6 (10), 1086–1095.

Schrenk, M.O., Brazelton, W.J., Lang, S.Q., 2013. Serpentinization, Carbon, and Deep Life. In: Carbon in Earth. Mineralogical Soc, Amer, pp. 575–606.

Schroeder, T., John, B.E., 2004. Strain localization on an oceanic detachment fault system, Atlantis Massif, 30°N, Mid-Atlantic Ridge. Geochem., Geophys., Geosyst. 11, Q11007.

Seewald, J.S., Zolotov, M.Y., McCollom, T., 2006. Experimental investigation of single carbon compounds under hydrothermal conditions. Geochim. Cosmochim. Acta 70 (2), 446–460.

Seyfried, W.E., Bischoff, J.L., 1979. Low temperature basalt alteration by seawater: an experimental study at 70°C and 150°C. Geochim. Cosmochim. Acta 43, 1937–1947.

Seyfried, W.E., Pester, N.J., Tutolo, B.M., Ding, K., 2015. The lost city hydrothermal system: constraints imposed by vent fluid chemistry and reaction path models on subseafloor heat and mass transfer processes. Geochim. Cosmochim. Acta 163, 59–79.

Sherwood Lollar, B., Heuer, V.B., McDermott, J., Tille, S., Warr, O., Moran, J.J., Telling, J., Hinrichs, K.-U., 2021. A window into the abiotic carbon cycle – Acetate and formate in fracture waters in 2.7 billion year-old host rocks of the Canadian Shield. Geochim. Cosmochim. Acta 294, 295–314.

Sherwood Lollar, B., Warr, O., Higgins, P.M., 2024. The Hidden Hydrogensphere: The Contributions of Deep Groundwater to the Planetary Water Cycle. Ann. Rev. Earth Planet. Sci. 52, 15.1–15.24. https://doi.org/10.1146/annurev-earth-040722-102252.

Shipboard Scientific Party (1998) Explanatory notes. In Fouquet, Y., Zierenberg, R.A., Miller, D.J., et al., Proceedings of the Ocean Drilling Program, Initial Reports, 169: College Station, TX (Ocean Drilling Program), 17–32. doi: 10.2973/odp.proc.ir.169.1998.

Shipboard Scientific Party, 1999. Leg 176 summary. In Dick, H.J.B., Natland, J.H., Miller, D.J., et al., Proceedings of the Ocean Drilling Program, Initial Reports, 176. College Station, TX (Ocean Drilling Program), 1–70. https://doi.org/10.2973/odp.proc.ir.176.101.1999.

Shipboard Scientific Party (2000) Explanatory notes. In Binns, R.A., Barriga, F.J.A.S., Miller, D.J., et al., Proceedings of the Ocean Drilling Program, Initial Reports, 193: College Station, TX (Ocean Drilling Program), 1–72. doi: 10.2973/odp.proc.ir.193.2002.

Shock, E.L., 1992. Chemical environments of submarine hydrothermal systems. In: Holm, N.G. (Ed.), Marine Hydrothermal Systems and the Origin of Life. Kluwer Academic, Dordrecht, The Netherlands, pp. 67–107.

Shock, E.L., 1995. Organic acids in hydrothermal solutions: Standard molal thermodynamic properties of carboxylic acids, and estimates of dissociation constants at high temperatures and pressures. Am. J. Sci. 295, 496–580.

Sleep, N.H., Meibom, A., Fridriksson, T., Coleman, R.G., Bird, D.K., 2004. H_2-rich fluids from serpentinization: geochemical and biotic implications. Proc. Nat. Acad. Sci 101 (35), 12818–12823.

Spiers, E., Schmidt, B., 2023. Variable salinity and hydrogen production in Europa's ocean. J. Geophys. Res. – Planets 128 (11). Article e2023JE008028.

Spizzico, M., 2005. Radium and radon content in the carbonate-rock aquifer of the southern Italian region of Apulia. Hydrogeol. J. 13, 493–505.

Stevens, T.O., McKinley, J.P., 1995. Lithoautotrophic microbial ecosystems in deep basalt aquifers. Science 270 (5235), 450–454.

Suda, K., Aze, T., Miyairi, Y., Yokoyama, Y., Matsui, Y., et al., 2022. The origin of methane in serpentinite-hosted hyperalkaline hot spring at Hakuba Happo, Japan: radiocarbon, methane isotopologue and noble gas isotope approaches. Earth Planet. Sci. Lett. 585, 117510.

Suzuki, S., Ishii, S., Wu, A., Cheung, A., Tenney, A., Wanger, G., Kuenen, J.G., Nealson, K. H., 2013. Microbial diversity in The Cedards, an ultrabasic, ultrareducing, and low salinity serpentinizing ecosystem. Proc. Nat. Acad. Soc. 110 (38), 15336–15341.

Suzuki, S., Ishii, S.I., Chadwick, G.L., Tanaka, Y., Kouzuma, A., Watanabe, K., Inagaki, F., Albertsen, M., Nielsen, P.H., Nealson, K.H., 2024. A non-methanogenic archaeon within the order *Methanocellales*. Nat. Commun. 15. Article 4858.

Szponar, N., Brazelton, W.J., Schrenk, M.O., Bower, D.M., Steele, A., Morril, P.L., 2013. Geochemistry of a continental site of serpentinization, the Tablelands Ophiolite, Gros Morne National Park: a Mars analogue. Icarus 224, 286–296.

Takabayashi, M., Hirakawa, Y., Kakegawa, T., Furukawa, Y., 2023. Abiotic formation of ribose 5'-phosphate from ribose and apatite with carbonate- and formate-rich solutions. Geochemical Journal 57, 134–142.

Takai, K., Nakamura, K., Toki, T., Tsunogai, U., Miyazaki, M., Miyazaki, J., Hirayama, H., Nakagawa, S., Nunoura, T., Horikoshi, K., 2008. Cell proliferation at 122 degrees C and isotopically heavy CH_4 production by a hyperthermophilic methanogen under high-pressure cultivation. Proc. Nat. Acad. Sci 105 (31), 10949–10954.

Taran, Y., Kliger, G., Cienfuegos, E., Shuykin, A., 2010. Carbon and hydrogen isotopic compositions of products of open-system catalytic hydrogenation of CO_2: implications for abiogenic hydrocarbons in Earth's crust. Geochim. Cosmochim. Acta 74, 6112–6125.

Templeton, A.S., Caro, T.A., 2023. The rock-hosted biosphere. Annu. Rev. Earth Planet. Sci. 51, 493–519.

Templeton, A.S., Ellison, E.T., Glombitza, C., Morono, Y., Rempfert, K.R., Hoehler, T.M., Zeigler, S.D., Kraus, E.A., Spear, J.R., Nothaft, D.B., Fones, E.M., Boyd, E.S., Munro-Ehrlich, M., Mayhew, L.E., Cardace, D., Matter, J.M., Kelemen, P.B., the Oman Drilling Project Science Party, 2021. Accessing the subsurface biosphere within rocks undergoing active low-temperature serpentinization in the Samail Ophiolite (Oman Drilling Project). J. Geophys. Res.: Biogeosci. 126, e2021JG006315. https://doi.org/10.1029/2021JG006315.

Templeton, A.S., Ellison, E.T., Kelemen, P.B., Leong, J., Boyd, E.S., Colman, D.R., Matter, J.M., 2024. Low-temperature hydrogen production and consumption in partially-hydrated peridotites in Oman: implications for stimulated geological hydrogen production. Front. Geochem. 2, 1366268.

Ternieten, L., Früh-Green, G.L., Bernasconi, S.M., 2021. Distribution and sources of carbon in serpentinized mantle peridotites at the Atlantis massif (IODP Expedition 357). J. Geophys. Res.: Solid Earth. 126, e2021JB021973.

Thirlwall, M.F., 1991. Long-term reproducibility of multicollector Sr and Nd isoope ratio analysis. Chem. Geol. 94 (2), 85–104.

Titarenko, S.S., McCaig, A.M., 2016. Modelling the lost city hydrothermal field: influence of topography and permeability structure. Geofluids 16 (2), 314–328.

Vance, S.D., Daswani, M.M., 2020. Serpentinite and the search for life beyond Earth. Phil. Trans. R. Soc. a. 378 (2165). Article 20180421.

Von Damm, K.L. and Lilley, M.D. (2004) Diffuse flow hydrothermal fluids from 9 50' N East Pacific Rise: Origin, Evolution and Biogeochemical Controls. The subseafloor Biosphere at Mid-Ocean Ridges. Geophysical Monograph Series 144.

Waite Jr, J.H., Combi, M.R., Ip, W.H., Cravens, T.E., McNutt Jr, R.L., Kasprzak, W., Yelle, R., Luhmann, J., Niemann, H., Gell, D., Magee, B., 2006. Cassini ion and neutral mass spectrometer: enceladus plume composition and structure. Science 311 (5766), 1419–1422.

Waite Jr, J.H., Lewis, W.S., Magee, B.A., Lunine, J.I., McKinnon, W.B., Glein, C.R., Mousis, O., Young, D.T., Brockwell, T., Westlake, J., Nguyen, M.J., 2009. Liquid water on Enceladus from observations of ammonia and 40Ar in the plume. Nature 460 (7254), 487–490.

Waite, J.H., Glein, C.R., Perryman, R.S., Teolis, B.D., Magee, B.A., Miller, G., Grimes, J., Perry, M.E., Miller, K.E., Bouquet, A., Lunine, J.I., 2017. Cassini finds molecular hydrogen in the Enceladus plume: evidence for hydrothermal processes. Science 356 (6334), 155–159.

Wang, D.T., Reeves, E.P., McDermott, J.M., Seewald, J.S., Ono, S., 2018. Clumped isotopologue constraints on the origin of methane at seafloor hot springs. Geochim. Cosmochim. Acta 223, 141–158.

Wang, J., Nitschke, F., Gholami Korzani, M., Kohl, T., 2019. Temperature log simulations in high-enthalpy boreholes. Geotherm. Energy 7 (1), 32. https://doi.org/10.1186/s40517-019-0149-0.

Wankel, S.D., Germanovich, L.N., Lilley, M.D., Genc, G., DiPerna, C.J., Bradley, A.D., Olson, E.J., Girguis, P.R., 2011. Influence of the subsurface biosphere on geochemical fluxes from diffuse hydrothermal fluids. Nat. Geosci 4, 461–468.

Wee, S.Y., Edgcomb, V.P., Beaudoin, D., Yvon-Lewis, S., Sylvan, J.B., 2021. Microbial abundance and diversity in subsurface lower oceanic crust at Atlantis Bank, Southwest Indian Ridge. Appl. Environ. Microbiol. 87 (22) e01519-21.

Weis, D., Kieffer, B., Maerschalk, C., Barling, J., de Jong, J., Williams, G.A., et al., 2006. High-precision isotopic characterization of USGS reference materials by TIMS and MC-ICP-MS. Geochem., Geophys., Geosyst. 7 (8), 1–30.

Zhao, Z., Feng, Q., Lu, H., Peng, P., Zhang, T., Hsu, C., 2021. Stable carbon isotopic fractionation and hydrocarbon generation mechanism of CO_2 Fischer-Tropsch-type synthesis under hydrothermal conditions. Energy Fuels 35, 11909–11919.